3341

$\pi\pi$ PHASE SHIFTS FROM $\pi^- p \to \pi^-\pi^+ n$ DATA*

A.D. Martin+ and P. Estabrooks†

CERN, Geneva.

*A talk based on the phase shift analysis of ref.(1).

+On leave of absence from the University of Durham, England.

†Supported by the National Research Council of Canada.

THIS PAGE

WAS INTENTIONALLY

LEFT BLANK

It was originally proposed[2] by Goebel and by Chew and Low that the $\pi N \to \pi\pi N$ cross section suitably extrapolated from the physical region to the π exchange pole ($t = \mu^2$) would provide a valuable means of determining the $\pi\pi$ differential cross section. Many attempts to extract $\pi\pi$ phases have been based on Chew-Low extrapolations, until now agreement has been reached on the general picture of the phases in the ρ region[3]. However, with the recent increase in experimental statistics of the $\pi^-p \to \pi^-\pi^+n$ data we are confronted with the problem of finding the best way to account for the other exchange mechanisms which are seen to occur in addition to π exchange. The method we propose is to use the observed moments of the $\pi^-\pi^+$ angular distribution to perform an amplitude analysis of the production process. In this way we can isolate the dominant π exchange amplitudes and extrapolate them to the π exchange pole. That we are able to perform such an amplitude analysis without knowledge of the nucleon polarization observables is a fortunate circumstance of the nature of the exchanges (see sections 2 and 3).

We use this method to extract $\pi\pi$ phase shifts from the high statistics $\pi^-p \to \pi^-\pi^+n$ data at 17.2 GeV/c[4]. We discuss separately the $\pi\pi$ phase shift analysis below and above the $K\bar{K}$ threshold. The former is described in sections 4, 5, 6 and the latter in section 7. In section 8, we comment on the behaviour of the solutions near the $K\bar{K}$ threshold. However, first let us look at some experimental $\pi^-\pi^+$ moments from the point of view of pure π exchange.

1 π EXCHANGE IN $\pi^-p \to \pi^-\pi^+n$ - A QUICK LOOK

Suppose that the reaction $\pi^-p \to \pi^-\pi^+n$ were mediated entirely by π exchange (cf. fig. 1). Then the differential cross section is of the form

$$\frac{d^3\sigma}{dt\, dM_{\pi\pi}\, d\Omega} = A \frac{-t}{(t-\mu^2)^2} \frac{d\sigma_{\pi\pi}}{d\Omega} \qquad (1)$$

where $d\sigma_{\pi\pi}/d\Omega$ is the $\pi^+\pi^-$ differential cross section in the $\pi^+\pi^-$ rest frame.

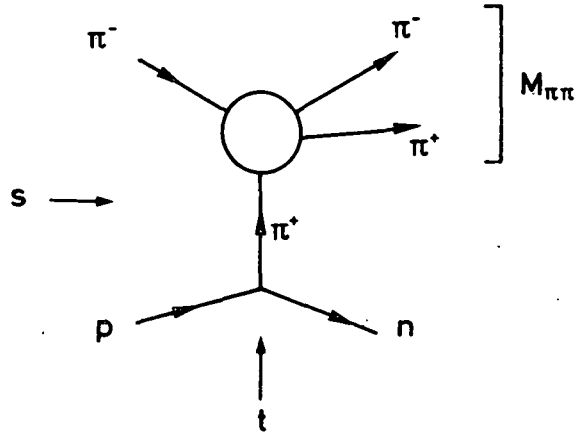

Fig. 1 π exchange in $\pi^- p \to \pi^- \pi^+ n$.

The factor t arises because the π flips the nucleon spin. For completeness we give

$$A = \frac{2}{4\pi\, m^2\, p_L^2} \frac{g^2}{4\pi} |F(t)|^2\, q\, M_{\pi\pi}^2 , \qquad (2)$$

where m is the nucleon mass, p_L the laboratory momentum, q the $\pi\pi$ c.m. momentum, $g^2/4\pi \approx 14$ and $F(t)$ a form factor satisfying $F(\mu^2) = 1$.

The experimental observables are the moments $\langle Y_M^J \rangle$ of the $\pi^-\pi^+$ angular distribution as a function of t and $M_{\pi\pi}$

$$\frac{d^3\sigma}{dt\, dM_{\pi\pi}\, d\Omega} = N \sum_J \sum_{M=-J}^{J} \langle Y_M^J \rangle \, \mathrm{Re}\, Y_M^J(\theta, \phi), \qquad (3)$$

where N is the number of events in the element $dt\, dM_{\pi\pi}$, and where we have chosen the y axis normal to the $\pi^- p \to (\pi\pi)n$ reaction plane. We use $\langle Y_M^J \rangle$ to abbreviate $\mathrm{Re} \langle Y_M^J \rangle$. On the other hand, we wish to calculate the $\pi\pi$ partial wave amplitudes $f_L(M_{\pi\pi})$

$$\frac{d\sigma_{\pi\pi}}{d\Omega} = \left| \frac{1}{q} \sum_L (2L+1)\, f_L\, P_L(\cos\theta) \right|^2 \qquad (4)$$

For $\pi^+\pi^-$ the isospin decomposition is

$$\begin{aligned} f_L &= 2/3\, f_L^{I=0} + 1/3\, f_L^{I=2} \quad \text{for even } L\,, \\ f_L &= f_L^{I=1} \qquad\qquad\qquad\quad \text{for odd } L\,. \end{aligned} \tag{5}$$

The f_L^I are defined so that in the $\pi\pi$ elastic region

$$f_L^I = \sin\delta_L^I \exp(i\,\delta_L^I)\,. \tag{6}$$

π exchange produces only (t-channel) helicity zero $\pi^-\pi^+$ systems, and in this simplified situation only the M = 0 moments, $\langle Y_0^J \rangle$, would be non-zero. We may express these moments in terms of the $\pi^-p \to \pi^-\pi^+n$ amplitudes for the production of S, P, ... wave helicity zero $\pi^-\pi^+$ states

$$\begin{aligned} \sqrt{4\pi}\, N\langle Y_0^0\rangle &= |S|^2 + |P_0|^2 + |D_0|^2 \\ \sqrt{4\pi}\, N\langle Y_0^1\rangle &= 2\,\mathrm{Re}\,(SP_0^*) + \frac{4}{\sqrt{5}}\,\mathrm{Re}\,(P_0\,D_0^*) \\ \sqrt{4\pi}\, N\langle Y_0^2\rangle &= \frac{2}{\sqrt{5}}|P_0|^2 + 2\,\mathrm{Re}\,(S\,D_0^*) + \frac{\sqrt{20}}{7}|D_0|^2 \\ \sqrt{4\pi}\, N\langle Y_0^3\rangle &= \sqrt{\frac{108}{35}}\,\mathrm{Re}\,(P_0\,D_0^*) \\ \sqrt{4\pi}\, N\langle Y_0^4\rangle &= \frac{6}{7}|D_0|^2 \end{aligned} \tag{7}$$

where we neglect F- and higher waves. Up to a normalization constant, the (helicity zero) production amplitudes S, P_0, D_0 are

$$L_0 = \frac{\sqrt{-t}}{t-\mu^2} F(t)\, \frac{M_{\pi\pi}}{\sqrt{q}}\, \sqrt{2L+1}\, f_L\,. \tag{8}$$

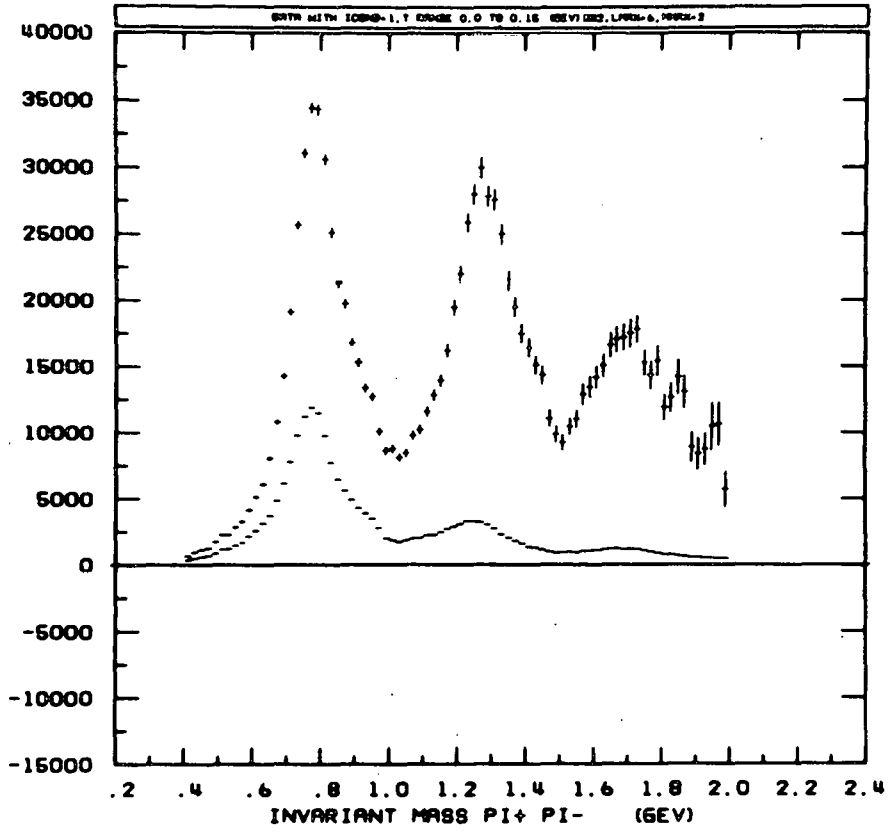

Fig. 2 The upper (lower) points are the corrected (uncorrected) number of events in $\Delta M_{\pi\pi}\ \Delta t$ bins with $\Delta M_{\pi\pi}$ = 20 MeV and $0 < -t < 0.15$ GeV^2, taken from ref. 5. The M = 1 moments are 2 N $\langle Y_M^J \rangle$ and not as labelled.

In figs. 2 and 3 we show the mass spectrum of the unnormalized t-channel moments integrated over the interval $0 < -t < 0.15$ GeV^2 obtained in the $\pi^- p \to \pi^- \pi^+ n$ CERN-Munich experiment[6] at 17.2 GeV/c. From these moments, we see

(a) the presence of the $\rho(770)$, f(1260), g(1700) mesons with spins 1, 2, 3 respectively; to establish[6,4] spin 3 for the g meson requires the additional knowledge that the J = 7 and higher moments are small near 1700 MeV;

(b) from $\langle Y_0^1 \rangle$ the presence of a large S-wave under the ρ-meson;

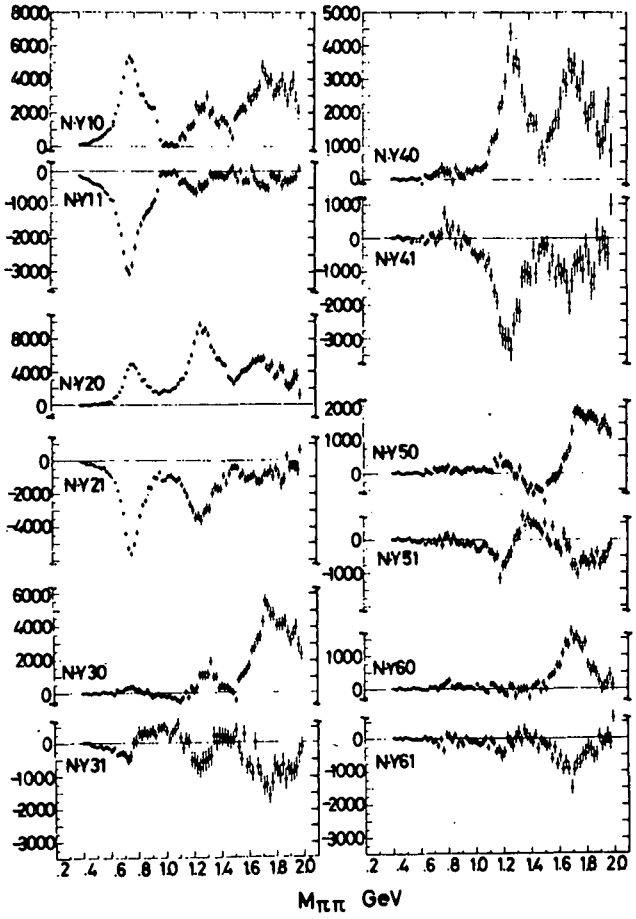

Fig. 3 The corrected unnormalized t-channel moments, $N\langle Y_M^J \rangle$, as a function of $\pi^+\pi^-$ mass for the interval $0 < -t < 0.15$ GeV^2, taken from ref. 5.

(c) from $\langle Y_0^2 \rangle$ the presence of a large S-wave under the f-meson[7];

(d) sharp structure near $M_{\pi\pi}$ = 1 and 1.45 GeV which Odorico[8] associates with the double pole killing zeros propagating linearly into the $\pi^-\pi^+$ physical region from the forward direction; the effect at 1 GeV is complicated by the opening of the $K\bar{K}$ channel with the cross section at its S-wave unitarity limit suggesting the nearby presence of the S* meson[9];

(e) from $\langle Y_1^J \rangle$ moments the non-negligible presence of helicity one $\pi^-\pi^+$ production.

It is illuminating to establish statement (c) above in the following way. From figs. 2 and 3 we see at the mass of the f-meson the relative sizes of the moments are

$$\langle Y_0^0 \rangle : \langle Y_0^1 \rangle : \langle Y_0^2 \rangle : \langle Y_0^3 \rangle : \langle Y_0^4 \rangle$$

$$8.5 \quad : \quad 2.5 \quad : \quad 9 \quad : \quad 1.5 \quad : \quad 4 \ .$$

However, assuming the dominance of D-wave $\pi\pi$ production we see from eqns.(7) that the ratios are expected to be

$$1 \quad : \quad 0 \quad : \quad 0.64 \quad : \quad 0 \quad : \quad 0.86 \ .$$

To enhance $\langle Y_0^2 \rangle$ to agree with the data we need to consider the D - S wave interference term. For example if S $\approx$ 0.8 D then the predicted ratios are in rough agreement with the data

$$1.64 \quad : \quad 0 \quad : \quad 2.24 \quad : \quad 0 \quad : \quad 0.86 \ .$$

However, in terms of partial waves (cf. eqn.(8))

$$\frac{S}{D} = \frac{f_S}{\sqrt{5}\, f_D}$$

Thus, assuming an elasticity of 0.8 for the f-meson and no I = 2 contributions, we anticipate that the S-wave will be at its unitarity limit and approximately in phase with D as shown in fig. 4. Even then S is only about 0.5 D.

So far we have assumed pure π exchange. If this were true few problems would exist in the extraction of $\pi\pi$ phases from the data. However, the sizeable $\langle Y_1^J \rangle$ moments of fig. 3 are a warning that other exchange mechanisms are present, such as A_2 exchange or absorptive corrections. Thus a $\pi\pi$ phase shift analysis based on a straightforward extrapolation of the $\langle Y_0^J \rangle$ moments can be very misleading[10]. Additional terms occur on the right-hand sides of

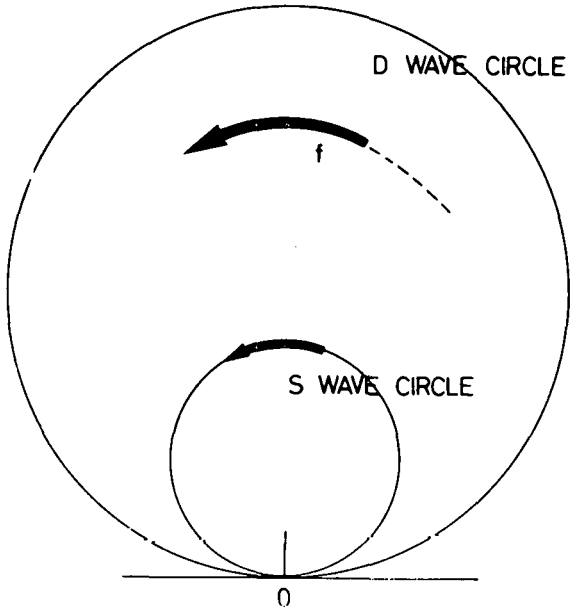

Fig. 4 Expectations of the $\pi\pi$ I = 0 S-wave in the region of the f resonance from a naive study of the $\langle Y_0^J \rangle$ moments. The unitarity circles are drawn for $\sqrt{2L+1}\, f_L$.

eqns.(7) involving amplitudes describing non-zero helicity $\pi\pi$ production. To allow for these other exchanges, we perform a production amplitude analysis of all the observed moments as functions of t and $M_{\pi\pi}$.

2 PRODUCTION AMPLITUDES AND OBSERVABLES FOR $\pi N \to \pi\pi N$

For the reaction $\pi^- p \to \pi^- \pi^+ n$ we use the variables shown in fig. 5.

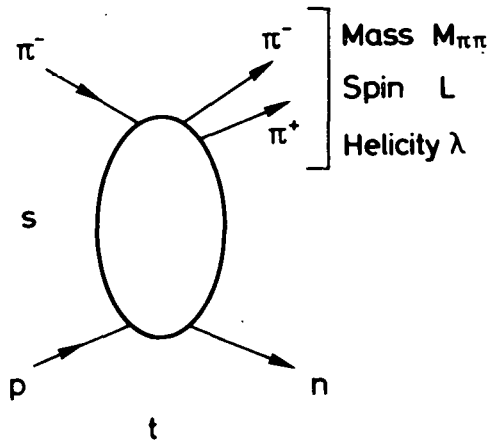

Fig. 5 Variables for the process $\pi^- p \to \pi^- \pi^+ n$.

The production of a $\pi^-\pi^+$ system of spin L is described by helicity amplitudes $H^{L,\lambda}(s, t, M^2_{\pi\pi})$ with helicity $\lambda = 0, \pm 1, \ldots, \pm L$. For the moment we omit the nucleon helicity labels. This simplifies the discussion and will be corrected for later.

It is convenient to introduce the combinations of helicity amplitudes

$$L_{\lambda\pm} = \frac{1}{\sqrt{2}} (H^{L,\lambda} \mp (-1)^{\lambda} H^{L,-\lambda}) . \tag{9a}$$

At high energies (that is, to order 1/s) the amplitudes $L_{\lambda+}$ and $L_{\lambda-}$ describe the production of a $\pi\pi$ system of spin L, helicity λ by natural and unnatural parity exchange, respectively. We see that $L_{\lambda+} = 0$ for $\lambda = 0$ $\pi\pi$ production, that is a zero helicity $\pi\pi$ system cannot be produced at high energies by natural parity exchange. In this case we have only an unnatural parity exchange amplitude, which we define as

$$L_0 \equiv H^{L,0} . \tag{9b}$$

At a given s, t and $M_{\pi\pi}$, the experimental observables are the moments $\langle Y^J_M \rangle$ of the $\pi^+\pi^-$ angular distribution with respect to some specified frame (cf. eqn.(3)). The two standard choices of axes, the s- and t-channel helicity frames, are shown in fig. 6. The observables in one frame can be obtained in the other by the transformation

$$\langle Y^J_M \rangle^{(s)} = \sum_{M'} d^J_{M'M}(\omega) \langle Y^J_{M'} \rangle^{(t)} \tag{10}$$

A useful (large s, small t) approximation for the crossing angle ω is

$$\cos\omega \approx \frac{M^2_{\pi\pi} + t}{M^2_{\pi\pi} - t} , \qquad \sin\omega \approx \frac{2\sqrt{-t}}{M_{\pi\pi}} . \tag{11}$$

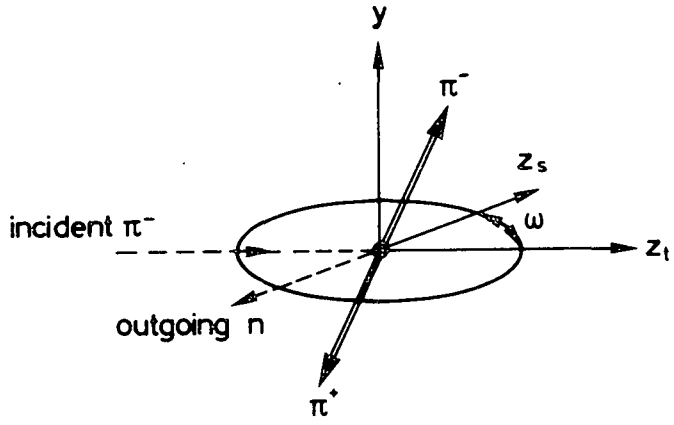

Fig. 6 The s- and t-channel axes used to describe the angular distribution of the produced $\pi^-\pi^+$ system as seen from its rest frame. The y axis is normal to the $\pi^- p \to (\pi\pi)n$ reaction plane. The two choices of the z axis are shown.

The crossing matrix for the helicity amplitudes is block diagonal in the combinations $L_{\lambda+}$ and $L_{\lambda-}$ formed in eqn.(9). The L "natural" parity exchange amplitudes have the crossing property

$$L^{(s)}_{\lambda+} = \sum_{\lambda' > 0} \left[d^{L}_{\lambda'\lambda}(\omega) - (-1)^{\lambda'} \, d^{L}_{-\lambda'\lambda}(\omega) \right] L^{(t)}_{\lambda'+} . \qquad (12)$$

Similarly the L + 1 "unnatural" parity exchange amplitudes, $L_{\lambda-}$, cross amongst themselves.

The observables $\langle Y^J_M \rangle$ may be expressed in terms of the amplitudes (S_0, P_0, $P_{1\pm}$, D_0, $D_{1\pm}$, $D_{2\pm}$, ...) of eqn.(9). Each moment is a sum over bilinear terms of the form Re (L'_λ, L^*_λ). A given moment $\langle Y^J_M \rangle$ will only contain terms with $L' + L \geq J$ and $| \lambda' - \lambda | = M$. Furthermore $L' + L$ must be even (odd) if J is even (odd). These restrictions are embodied in the Clebsch-Gordan coefficients $\langle LL' \; \lambda - \lambda' \mid JM \rangle$ and $\langle LL'00 \mid J0 \rangle$ which occur when the density matrix is expressed in terms of the moments[11]. Moreover, the moments contain no interference terms between $L_{\lambda+}$ and $L_{\lambda-}$ amplitudes.

For example, in a region of $M_{\pi\pi}$ where only S and P wave $\pi\pi$ production is appreciable, the observables can be expressed in terms of the production

amplitudes S_0, P_0, $P_{1\pm}$ as follows

$$\begin{aligned}
\sqrt{4\pi}\, N \langle Y_0^0 \rangle &= |S|^2 + |P_0|^2 + |P_+|^2 + |P_-|^2 \\
\sqrt{4\pi}\, N \langle Y_0^1 \rangle &= 2\, \mathrm{Re}\, (S P_0^*) \\
\sqrt{4\pi}\, N \langle Y_1^1 \rangle &= \sqrt{2}\, \mathrm{Re}\, (S P_-^*) \\
\sqrt{4\pi}\, N \langle Y_0^2 \rangle &= \frac{1}{\sqrt{5}} (2\, |P_0|^2 - |P_+|^2 - |P_-|^2) \\
\sqrt{4\pi}\, N \langle Y_1^2 \rangle &= \sqrt{\frac{6}{5}}\, \mathrm{Re}\, (P_0\, P_-^*) \\
\sqrt{4\pi}\, N \langle Y_2^2 \rangle &= -\sqrt{\frac{3}{10}}\, (|P_+|^2 - |P_-|^2) \, .
\end{aligned} \tag{13}$$

So far we have simplified the discussion by disregarding the nucleon helicities. Each amplitude is really two independent amplitudes, a nucleon helicity flip and a non-flip amplitude $H^{L,\lambda}_{+-}$ and $H^{L,\lambda}_{++}$, respectively. The combinations of eqn.(9) are to be formed for both the nucleon flip and non-flip amplitudes. For an experiment involving unpolarized nucleons, eqns.(13) are correct provided it is understood that the nucleon helicities are summed over as follows

$$\begin{aligned}
|L|^2 &\equiv |L_{++}|^2 + |L_{+-}|^2 \\
\mathrm{Re}\, (L'L^*) &\equiv \mathrm{Re}\, (L'_{++}\, L^*_{++} + L'_{+-}\, L^*_{+-}) \, .
\end{aligned} \tag{14}$$

Here we have omitted the $\pi\pi$ helicity label. Furthermore the crossing relations, eqn.(12), are unchanged.

In conclusion, we see that when we analyze an unpolarized nucleon experiment we need only treat the spin of the $\pi\pi$ system explicitly, provided we make an incoherent sum over the nucleon helicities. When nucleon polarization measurements are available, we can study the nucleon non-flip and flip amplitudes separately and, moreover, observe interference effects between $L_{\lambda+}$ and $L_{\lambda-}$ amplitudes.

3 EXCHANGE MECHANISMS

The absence of nucleon polarization data prevents a model independent determination of the amplitudes for $\pi N \to (\pi\pi)N$. However, the unnatural parity exchanges have the simplifying property* that π exchange contributes only to nucleon flip amplitudes, whereas the amplitudes with the quantum numbers of A_1 exchange have nucleon non-flip (cf. Table 1). We shall call the latter A_1 exchange contributions regardless of whether they arise from A_1 exchange, absorption, etc., with the exception of the order $1/s$ π exchange contribution in the s-channel which we include explicitly. It is reasonable to assume that the non-flip A_1 exchange is negligible in comparison to the π exchange flip amplitudes, particularly as the neglected quantities only enter quadratically in the expressions for the observables $\langle Y_M^J \rangle$, that is there are no π - A_1 interference terms.

The most direct check of this assumption will be nucleon polarization measurements for $\pi N \to \pi\pi N$; the polarization associated with unnatural parity exchange is due to π - A_1 interference. Another check is the measurement of both the target and recoil polarization for $\gamma p \to \pi^+ n$; $P_T = P_R$ would imply that the A_1 exchange amplitude $H^1_{++} - H^{-1}_{++}$ is zero[12]. Also we can check the small t-dependence of the observable $(3\,\rho^P_{00} + \rho^S_{00})\,d\sigma/dt$ in a $\pi\pi$ mass region where S- and P-waves are dominant. The π exchange contribution vanishes like t in contrast to the non-flip A_1 contribution. In practice this test[13] is difficult, requiring very high statistics and depending mainly on the extreme forward data points. Finally, by considering the eigenvalues of the density matrix within the positivity domain, bounds can be obtained for the A_1 type contributions[14].

With the assumption of negligible A_1 exchange contributions it follows, for example, that the relative phases

$$\begin{aligned} \phi &= \arg(P_-) - \arg(P_0) \\ \Delta &= \arg(S_0) - \arg(P_0) \end{aligned} \qquad (15)$$

---

*This is exactly true for π exchange in the t-channel; in the s-channel we have order $1/s$ π exchange contributions to the nucleon non-flip amplitudes.

TABLE 1

Regge exchange contributions to the s-channel helicity amplitudes for $\pi^- p \to (\pi^-\pi^+)n$ and their behaviour in the forward direction, $t' \equiv t - t_{min} = 0$. λ is the helicity of the $\pi^-\pi^+$ system. The amplitudes $L_{\lambda+}$ and $L_{\lambda-}$ are defined in eqns.(9). To leading order in s, only the exchanges listed contribute to $L_{\lambda+}$ and $L_{\lambda-}$.

s ch. hel. amp. $H^{L,\lambda}_{\lambda_n,\lambda_p}$	n, x	ang. mom. $(\sqrt{-t'})^n$	Regge pole exchange	
			nat. p. ($L_{\lambda+}$) unnat. p. ($L_{\lambda-}$)	$(\sqrt{-t'})^{n+x}$
$H^{L,0}_{+-}$	1 0	$\sqrt{-t'}$	π	$\sqrt{-t'}$
$H^{L,0}_{++}$	0 0	const.	A_1	const.
$H^{L,1}_{+-}$	0 2	const.	$A_2 + \pi$	$-t'$
$H^{L,-1}_{+-}$	2 0	t'	$A_2 - \pi$	$-t'$
$H^{L,1}_{++}$	1 0	$\sqrt{-t'}$	$A_2 + A_1$	$\sqrt{-t'}$
$H^{L,-1}_{++}$	1 0	$\sqrt{-t'}$	$A_2 - A_1$	$\sqrt{-t'}$
$H^{L,2}_{+-}$	1 2	$\sqrt{-t'}$	$A_2 + \pi$	$(\sqrt{-t'})^3$
$H^{L,-2}_{+-}$	3 0	$(\sqrt{-t'})^3$	$-A_2 + \pi$	$(\sqrt{-t'})^3$
.				
.				
.				

determine the phase between S_0 and P_-. Thus in a region of $M_{\pi\pi}$ where only S and P wave $\pi^-\pi^+$ states are important we can use the six observable moments, eqns.(13), to determine[15] $|P_+|$, $|P_0|$, $|P_-|$, $|S|$, ϕ and Δ as functions of $M_{\pi\pi}$ and t. In section 4 we discuss the uniqueness of the solution and also how we include the small D-wave contribution.

3.1 Choice of Frame and Absorptive Corrections

In order to extract $\pi\pi$ phase shifts we must isolate the $\pi N \to (\pi\pi)N$ amplitudes which are dominated by π pole exchange and suitably extrapolate them from the physical region to $t = \mu^2$. Clearly S_0, P_0, D_0, ... are the desired amplitudes. Now the amplitude analysis can be done equally well using either the s- or t-channel moments of the $\pi^+\pi^-$ angular distribution (cf. fig. 6). However, we argue that it is appropriate to extrapolate s-channel amplitudes. The reason is that we believe the absorptive corrections to the exchange pole contributions are simpler in the s-channel[16]. At present we do not have a reliable prescription for determining these corrections. The indications are that they interfere destructively with the pole contributions and that, to a good approximation, they conserve s-channel helicities. Moreover, they are expected to be largest in $x \neq 0$ s-channel amplitudes, and, for $x = 0$ amplitudes, to decrease with increasing net helicity flip n. For an s-channel helicity amplitude the net helicity flip, $n = |\lambda + \lambda_p - \lambda_n|$, specified the forward behaviour arising from angular momentum conservation, and $n + x = |\lambda| + |\lambda_p - \lambda_n|$ specifies the behaviour for definite parity (Regge pole) exchange. This behaviour, together with the values of n and x, is listed in Table 1.

Consider the $x = 2$ $H^{L,1}_{+-}$ s-channel helicity amplitude. The pole contributions, which are required to vanish as t', are expected to be modified by destructive interference with a non-vanishing (absorptive) background. The cross-over zeros in the s-channel $\langle Y^J_1 \rangle$ moments near $-t = \mu^2$ are experimental support for this picture. This absorptive correction to the s-channel P_{1-}, D_{1-}, ... amplitudes will, when crossed, affect the t-channel P_0, D_0, ... amplitudes. Of course, the s-channel S_0, P_0, ... amplitudes may themselves have absorptive corrections, but as these are helicity flip amplitudes these modifications should be relatively small. In either channel the absorptive modifications to S_0, P_0, D_0, ... do not in principle cause a problem since they should disappear on appropriate extrapolation to the π exchange pole. However, to determine $\pi\pi$

phases it is desirable to extrapolate what are believed to be the "purest" π exchange amplitudes and for this reason we shall use the s-channel S_0, P_0, D_0, ... amplitudes.

One slight complication of this choice is that the π pole contribution, which in the t-channel contributes only to S_0, P_0, ..., is distributed among all the $L_{\lambda-}$ s-channel amplitudes. For example, for P wave $\pi^+\pi^-$ production we have to leading order in s

$$(P_0)_{+-} \equiv H^{1,0}_{+-} = -\frac{g_\pi}{\sqrt{q}} \frac{t + M^2_{\pi\pi} - \mu^2}{M_{\pi\pi}} \frac{\sqrt{-t'}}{t - \mu^2}$$

$$P_- = \frac{g_\pi}{\sqrt{q}} \frac{2t'}{t - \mu^2} \qquad (16)$$

$$(P_0)_{++} \equiv H^{1,0}_{++} = r\, H^{1,0}_{+-} \quad \text{with} \quad r = \sqrt{t_{min}/t'}$$

The last amplitude is only relevant at very small t. To include its contribution we multiply each product of $\lambda = 0$ amplitudes (e.g. $|P_0|^2$, $\mathrm{Re}(S_0 P_0^*)$) occurring in the expressions for the observable moments, eqns.(13), by $1 + r^2$ before solving for the amplitudes[15]. Thus from now on by S_0, P_0, ... we mean only the helicity flip amplitudes $H^{L,0}_{+-}$.

4 PRODUCTION AMPLITUDE ANALYSIS FOR $M_{\pi\pi}$ BELOW 1 GeV

We have seen that the neglect of A_1 exchange amplitudes permits the determination of the magnitudes and relative phases of the amplitudes (S, P_0, P_-) and the magnitude of P_+ directly from the data. Instead of using the relative phases ϕ and Δ of eqn.(15) it is convenient to project S and P_- into components parallel and perpendicular to P_0 on the Argand plot, as illustrated in fig. 7. In terms of these amplitude components the moments of the $\pi^-\pi^+$

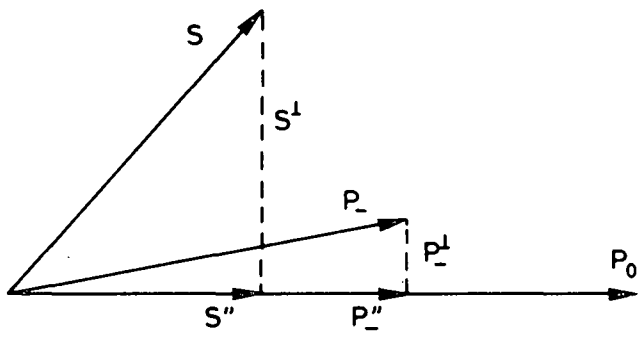

Fig. 7 Vectors representing the unnatural parity exchange amplitudes. The components S'', P_-'' and P_0 are well determined by the data, whereas essentially only the product of the perpendicular components, $P_-^{\perp}\, S^{\perp}$, is measured.

angular distribution becomes

$$
\begin{aligned}
\sqrt{4\pi}\, N \langle Y_0^0 \rangle &= |S''|^2 + |S^{\perp}|^2 + |P_0|^2 + |P_+|^2 + |P_-''|^2 + |P_-^{\perp}|^2 \\
\sqrt{4\pi}\, N \langle Y_0^1 \rangle &= 2\, S''\, |P_0| \\
\sqrt{4\pi}\, N \langle Y_1^1 \rangle &= \sqrt{2}\, (S''\, P_-'' + S^{\perp}\, P_-^{\perp}) \\
\sqrt{4\pi}\, N \langle Y_0^2 \rangle &= \frac{1}{\sqrt{5}} (2\, |P_0|^2 - |P_+|^2 - |P_-''|^2 - |P_-^{\perp}|^2) \\
\sqrt{4\pi}\, N \langle Y_1^2 \rangle &= \sqrt{\frac{6}{5}}\; P_-''\, |P_0| \\
\sqrt{4\pi}\, N \langle Y_2^2 \rangle &= -\sqrt{\frac{3}{10}}\; (|P_+|^2 - |P_-''|^2 - |P_-^{\perp}|^2)\,.
\end{aligned}
\tag{17}
$$

Eliminating all amplitude components in favour of $|P_0|$ we obtain a cubic equation for $|P_0|^2$. One solution is unphysical, $|P_0|^2 < 0$, and the remaining two solutions are both physical with similar values of $|P_0|^2$.

We are considering a region of $M_{\pi\pi}$ where D-waves are relatively small. Although in eqns.(17) we have omitted the terms depending on the D-wave amplitudes we do, in fact, allow for these small contributions. In the first place we solve for the two solutions using $\langle Y_0^1 \rangle - \sqrt{\frac{28}{27}} \langle Y_0^3 \rangle$ instead of $\langle Y_0^1 \rangle$ since, unlike $\langle Y_0^1 \rangle$, this combination does not contain the dominant D-wave

interference term Re $(P_0 D_0^*)$. Moreover, using the $\langle Y_0^3 \rangle$ moment we estimate D_0, $D_{1\pm}$ as described in section 5.2. We allow for these small D-wave contributions in the S- and P-wave amplitude analysis by iteration starting from the two exact solutions.

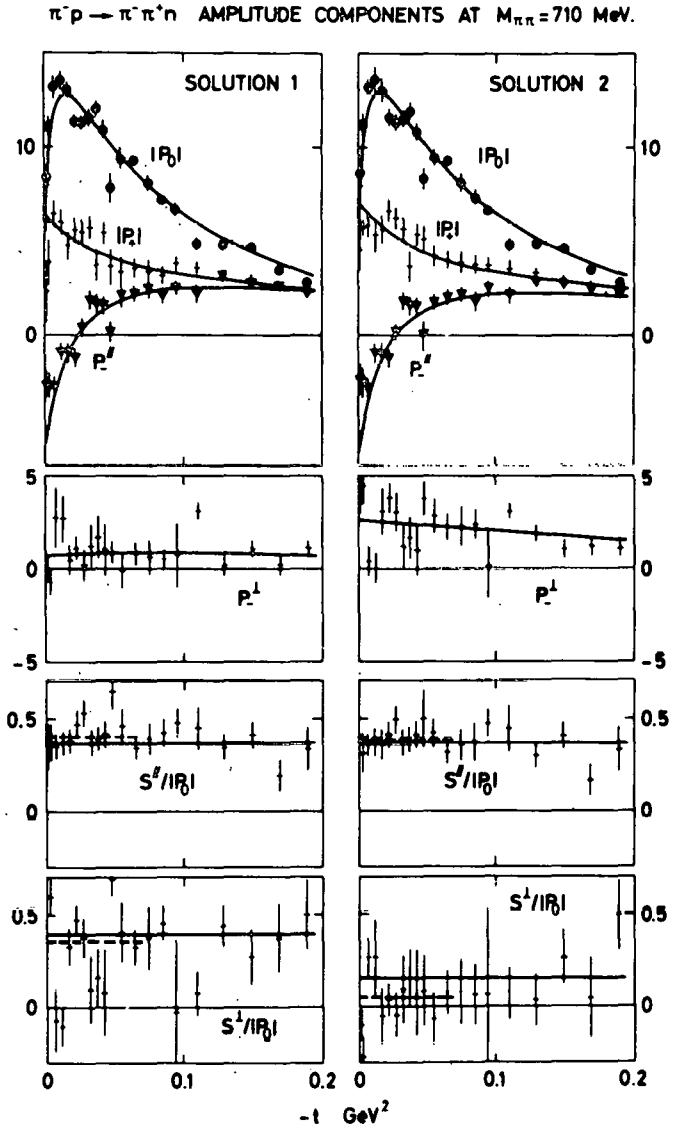

Fig. 8 The two solutions for the s-channel amplitude components calculated from the data in the mass bin $700 < M_{\pi\pi} < 720$ MeV. The points are the solutions obtained at the different t values and the dashed lines represent the resulting average values of S/P_0. The continuous lines are obtained from the parametric fit to the data that is described in section 5.

As an example we show in fig. 8 the two solutions found at the different t-values from the s-channel moments in the mass bin $700 < M_{\pi\pi} < 720$ MeV as measured by the CERN-Munich collaboration[4]. The amplitudes S and P have similar t behaviour and so we show $Y_S'' = S''/|P_0|$ and $Y_S^{\perp} = S^{\perp}/|P_0|$. By

inspection of eqns.(17) we notice that the component $S^{\perp}$ is less constrained than S'' and this is reflected in the resulting errors. Similarly the component P_-'' is better determined than $P_-^{\perp}$. Moreover the data do not determine the absolute signs of $S^{\perp}$ and $P_-^{\perp}$, but only their relative sign. In the ambiguous cases we have chosen $P_-^{\perp}$ to be positive in fig. 8.

We may compare the structure of these amplitude components with the behaviour anticipated from the contributions of π exchange to P_0 and P_- and A_2 exchange to P_+ (cf. section 3). Up to slope factors of the form $\exp\left[\, b(t - \mu^2)\,\right]$, the P-wave amplitudes are expected to have the following structure

$$P_0 = - g_\pi \; \tau_\pi \; M_{\pi\pi} \; \frac{\sqrt{-t'}}{t - \mu^2}$$

$$P_- = g_\pi \left[\tau_\pi \; \frac{2t'}{t - \mu^2} - C(t) \right] \qquad (18)$$

$$|P_+|^2 = \left| - t' \; g_A^F \; \tau_A - g_\pi \; C(t) \right|^2 - t' \left| g_A^{NF} \; \tau_A \right|^2$$

to leading order in s, where τ_i are signature factors $1/2 + 1/2 \exp(-i\pi\alpha_i)$ with $\alpha_\pi \approx t$ and $\alpha_A \approx 0.5 + t$, and g_A^F and g_A^{NF} are the A_2 exchange couplings to nucleon helicity flip and non-flip respectively. Studies[17] of ρ and A_2 exchange in spin 0 - spin 1/2 processes indicate that there $g_A^F/g_A^{NF} \approx 4$. The additional contribution $g_\pi \; C(t)$, which is non-vanishing at $t' = 0$, can be regarded as the absorptive correction to π and A_2 exchange in the (evasive) s-channel H^1_{+-} amplitude. At $t' = 0$ we have $P_+ = P_-$. The Williams' model[18] is a special case of eqns.(18), namely that with $g_A^{F,NF} = 0$, $\tau_\pi = 1$ and $C = 1$.

For the amplitudes obtained from the data in the ρ mass band, $730 < M_{\pi\pi} < 810$ MeV, such a breakdown has been discussed in ref. 15 (see also refs. 19 and 20). The actual interpretation of the various contributions to $P_\pm$ is not important as far as the extraction of $\pi\pi$ phases is concerned. However $P_\pm$ give sizeable contributions to the moments and it is crucial to allow for their presence in the Chew-Low extrapolation.

The two allowed solutions for the amplitude components are distinguished mainly by their differing values of S^1 and this leads to an ambiguity in the determination of the $\pi\pi$ S-wave phase.

4.1 Connection with $\pi\pi$ Phases

For each $M_{\pi\pi}$ bin the dominant π exchange amplitudes, S and P_0, are the appropriate quantities to extrapolate in t to $t = \mu^2$ to determine $\pi\pi$ phase shifts. We discuss first the P- wave and then the S-wave extrapolation.

To extrapolate $|P_0|$ to the π exchange pole we fit the calculated amplitudes for $-t < 0.2$ to the form (cf. eqn.(8))

$$P_0 = A \frac{\sqrt{-t'}}{\mu^2 - t} e^{b(t-\mu^2)} \sqrt{3}\, f_p \qquad (19)$$

where for $M_{\pi\pi}$ in the $\pi^-\pi^+$ elastic region $f_p = \sin\delta_p\, e^{i\delta_p}$. In other words from $|P_0|$ we determine $A\,|f_p|$ and thus knowing the normalization A we obtain δ_p the P-wave $\pi\pi$ phase shift. The normalization factor A has an $M_{\pi\pi}$ dependence

$$A^2 = N \frac{M_{\pi\pi}^2}{q} \left[\frac{M_{\pi\pi}^2}{M_{\pi\pi}^2 - 4\mu^2}\right] \qquad (20)$$

where $M_{\pi\pi}^2/q$ arises from the Chew-Low formula and the factor in brackets is due to crossing P_0 from the t- to the s-channel at $t = \mu^2$. It remains to fix the overall normalization constant, N, of the $\pi^-p \to \pi^-\pi^+n$ cross section $d\sigma/dM_{\pi\pi}$. To do this we extrapolate $|P_0|$ for each $M_{\pi\pi}$ bin in the region of the ρ resonance, and adjust the constant N until the resulting δ_p goes smoothly through the resonance. Knowing the constant N, and therefore A, we can calculate δ_p as a function of $M_{\pi\pi}$ in the $\pi^-\pi^+$ elastic region.

Consider now the extrapolation of the S-wave amplitude. To a good approximation the values of S/P_0 are constant in t. Therefore, to obtain the value at $t = \mu^2$, we simply fit the values for $-t < 0.2$ to a constant

$$\frac{S}{P_0} = \frac{2/3\, f_S^0 + 1/3\, f_S^2}{\sqrt{3}\, f_p} \qquad (21)$$

At the sample energy, $M_{\pi\pi}$ = 710 MeV, the resulting extrapolations for S''/P_0 and $S^{\perp}/P_0$ are indicated by dashed lines on fig. 8.

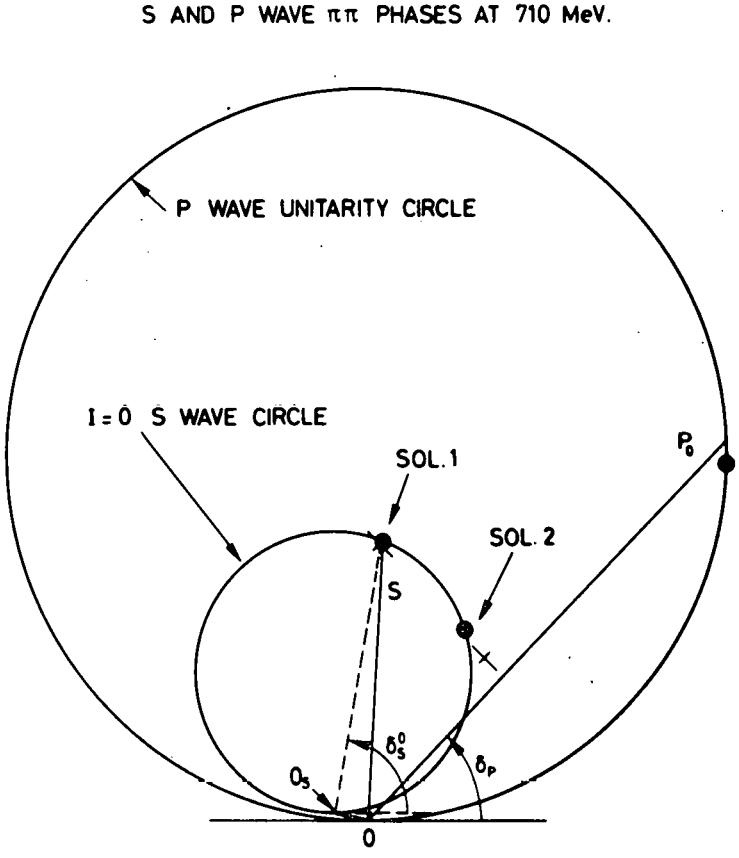

Fig. 9 The S- and P-wave $\pi\pi$ phases at $M_{\pi\pi}$ = 710 MeV obtained by extrapolating the amplitude solutions of fig. 8. The scale of the unitarity circles ($1 : 2/3\sqrt{3}$) represents the relative size of the amplitudes in the production process. The length OO_S is the input I = 2 S-wave. The crosses are the S-wave results obtained from the dashed lines of fig. 8. The black dots are the results of the parametric fit with elastic unitarity imposed.

It is illuminating to view the results in terms of the unitarity circles for the $\pi\pi$ partial wave amplitudes, f_L^I. We cannot determine both the I = 0 and I = 2 S wave $\pi\pi$ phase shifts and so we input f_S^2 using the values obtained in analyses[3,21] of $\pi^+p \to \pi^+\pi^+n$ data. The values we use for δ_S^2 are listed in Table 2. The situation at 710 MeV is shown in fig. 9. The larger unitarity circle corresponds to the P-wave which we assume to be elastic. Then, as described above, $|P_0|$ determines δ_P. The P-wave results for the two solutions are almost identical and are shown by a single line on fig. 9. Also we show the unitarity circle for the I = 0 S-wave, scaled down by the factor $2/3\sqrt{3}$ arising from $\sqrt{2L+1}$ and isospin. The shift of origin from 0 to O_S is due to the input I = 2 S-wave amplitude f_S^2. Knowing S''/P_0 and $S^{\perp}/P_0$ we may plot the S-wave

amplitude on fig. 9. The two solutions are indicated by crosses which represent their error bars. If the S-wave is elastic, as we expect, then the cross representing the physical solution should be on the unitarity circle. We notice that the well determined component S'' is similar for the two solutions, whereas the poorly known component $S^{\perp}$ distinguishes the two solutions. It is apparent that it is not going to be easy to select the physical solution for δ_S^0 simply from an analysis of $\pi^-p \to \pi^-\pi^+n$ data alone. As in previous analyses[3,5,22-24], we will have to take care to keep track of both solutions as a function of $M_{\pi\pi}$. Essentially the M = 0 moments determine $|P_0|$, S'' and $|S|^2 + |P_0|^2$ and so the best chance of getting a unique δ_S^0 appears to be in a region away from the ρ where $|S|$ is significantly different for the two solutions and leads to different extrapolated cross sections. The inclusion of the $M \neq 0$ moments is necessary to allow a reliable determination of P_0 and S. Moreover, in principle, from a knowledge of the sign of $P_-^{\perp}$, they also allow the sign of $S^{\perp}$ to be determined (cf. $\langle Y_1^1 \rangle$). In practice $P_-^{\perp}$ is small and poorly determined and so is not decisive.

So far S-wave unitarity has not been imposed. At first sight it appears that this could select the physical solution - perhaps one solution is always nearer to the circle than the other solution. However, $S^{\perp}$, like $P_-^{\perp}$, is badly determined and it would be misleading to select the solution in this way. Rather at the outset we should impose unitarity (at $t = \mu^2$) on the analysis and then see if one solution is preferred to the other. We describe such an analysis below.

5 $\pi\pi$ PHASE SHIFT ANALYSIS FOR $M_{\pi\pi}$ BELOW 1 GeV

The analysis is based on the high statistics $\pi^-p \to \pi^-\pi^+n$ data obtained by the CERN-Munich collaboration[4] at a laboratory momentum of 17.2 GeV/c. S-channel moments of the $\pi^-\pi^+$ angular distribution are used in 20 MeV $\pi\pi$ mass bins from $M_{\pi\pi}$ = 440 MeV upwards. In each mass bin we determine the structure of the production amplitudes in the range $0 < -t < 0.2$ GeV^2 by fitting the data to parametric forms based on eqns.(18). We include D-waves as outlined in section 4. We impose elastic unitarity, $f_L = \sin\delta_L \, e^{i\delta_L}$, through eqns.(19) and (21), except that, above the onset of the $\pi\omega$-channel, $M_{\pi\pi}$ = 920 MeV, we allow the P-wave to be inelastic.

The unitarity constraint is only true at $t = \mu^2$. However, we included a term $[1 + a(t - \mu^2)]$ on the right-hand side of eqn.(21). Since the unitarity phase is preserved[25] we took the parameter a to be real. Such a term could also arise from differing amounts of absorption in the π pole contributions to S and P_0, or from a t-dependence associated with crossing from the t- to the s-channel. The values found for the parameter a in the different mass bins were distributed about zero, and typically a $\lesssim \pm 0.5$ GeV^{-2}. The results we present have a = 0. Values of a = $\pm$ 0.5 lead to changes in δ_S^0 and δ_P of about $\pm 2^\circ$ and $\pm 0.5^\circ$ respectively.

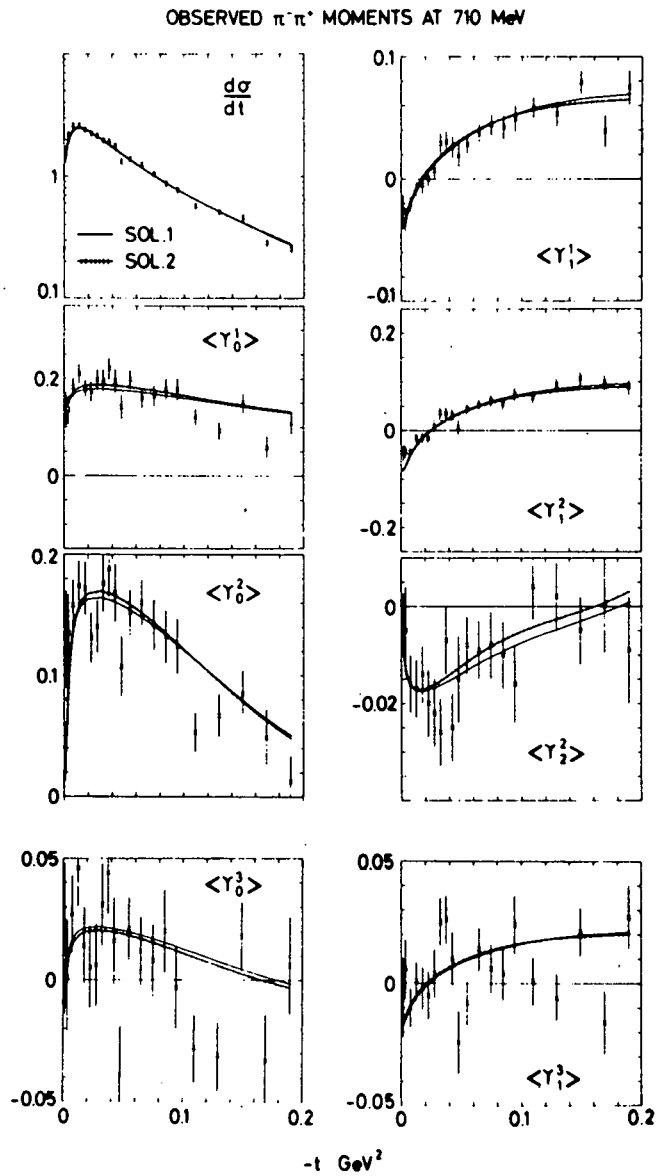

Fig. 10 The fits to the s-channel moments with $J \leq 2$ at $M_{\pi\pi}$ = 710 MeV corresponding to Solutions 1 and 2 of Table 2. The description of the J = 3 moments is also shown ($\delta_D^0 = 4.5^\circ$).

We tried several different forms of amplitude parametrization, allowing different slope factors $\exp[b(t - \mu^2)]$ on individual contributions, using different input values of g_A^F/g_A^{NF}, etc. The phase shift results were extremely stable to such changes of parametrization. We also repeated the analysis using only the data for $-t < 0.1$. Again the results were essentially unaltered. The curves shown in fig. 8 are the form of the amplitudes at 710 MeV. We see that they are a good description of the amplitude components determined t by t indicating that the chosen parametric form is adequate. The fit to the observed s-channel moments is shown in fig. 10.

5.1 S- and P-Wave $\pi\pi$ Phases

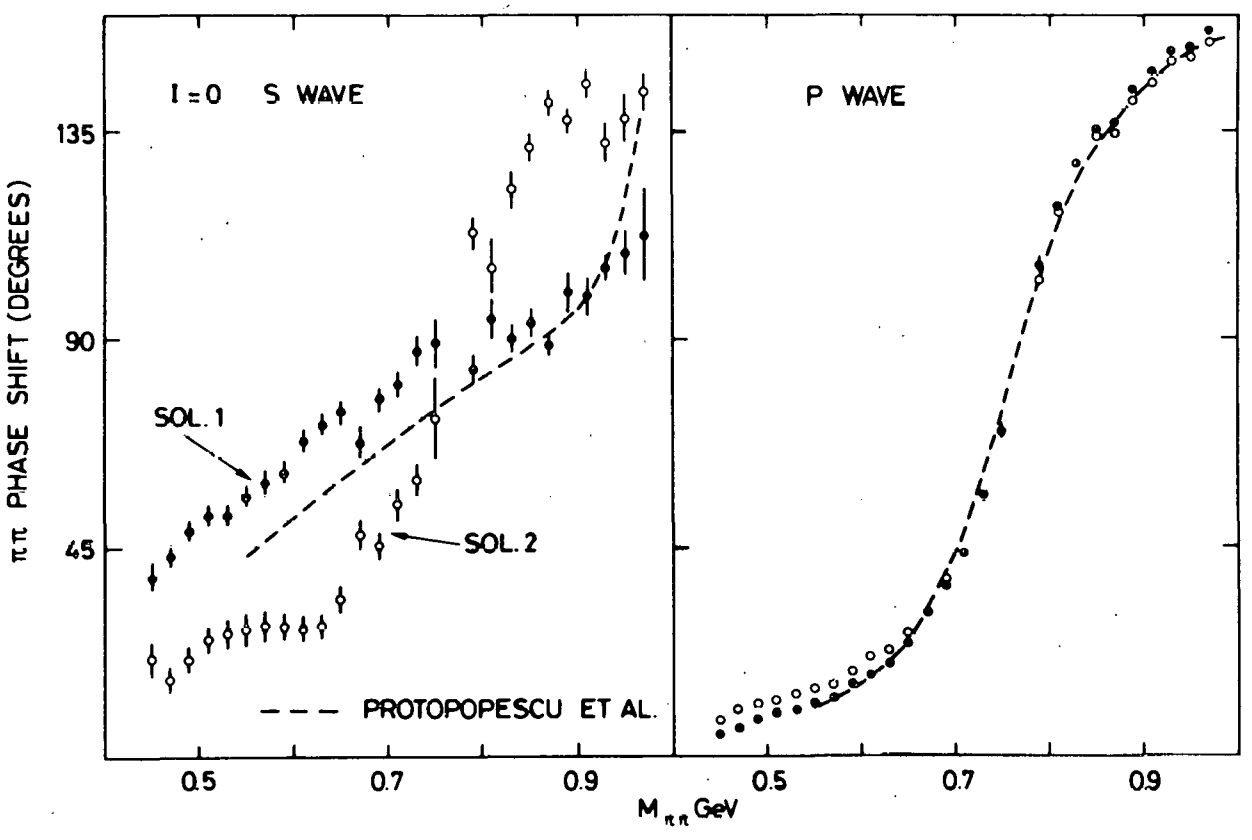

Fig. 11 The S- and P-wave $\pi\pi$ phase shifts, δ_S^0 and δ_P, below 1 GeV determined from the $\pi^- p \to \pi^-\pi^+ n$ amplitudes. The values are listed in Table 2. Solution 1 is the physical solution. For comparison the dashed line is the favoured solution obtained by Protopopescu et al.[24].

The phase shifts obtained by the method outlined above are shown in fig.11 and listed in Table 2. There are two solutions mainly differing in the values of δ_S^0. Solution 1 is characterized by a small P_-' and Solution 2 by a small S'.

TABLE 2

$\pi\pi$ Phase Shifts, δ_L^I in degrees determined from $\pi^- p \to \pi^-\pi^+ n$ data at 17.2 GeV/c in 20 MeV $\pi\pi$ mass bins. In each mass bin below 900 MeV six moments were fitted at 20 t values ($-t < 0.2$ GeV^2). Above 900 MeV 15 moments were used at the 20 t values. The $\pi^0\pi^0$ mass distribution selects Solution 1 as the physical solution.

$M_{\pi\pi}$	Solution 1				Solution 2				Input
(MeV)	δ_S^0	δ_P	δ_D^0	χ^2	δ_S^0	δ_P	δ_D^0	χ^2	δ_S^2
450	39.1 ± 2.7	4.8 ± 0.9	0.4	101	21.0 ± 3.4	7.6 ± 0.5	0.4	96	- 5.2
470	43.1 ± 1.8	6.2 ± 0.6	0.6	104	16.7 ± 2.4	9.9 ± 0.4	0.6	96	- 6.0
490	48.5 ± 2.0	7.9 ± 0.4	0.8	117	20.8 ± 2.6	11.5 ± 0.5	0.8	118	- 6.6
510	51.8 ± 2.2	9.3 ± 0.5	1.1	136	25.2 ± 2.7	12.2 ± 0.5	1.1	140	- 7.2
530	52.0 ± 2.2	10.0 ± 0.6	1.5	149	26.6 ± 3.3	13.1 ± 0.5	1.5	157	- 7.8
550	55.9 ± 2.3	11.5 ± 0.5	1.9	94	27.4 ± 3.5	14.6 ± 0.5	1.9	109	- 8.5
570	59.1 ± 2.7	12.5 ± 0.5	2.4	141	28.0 ± 3.6	15.3 ± 0.5	2.4	153	- 9.1
590	61.3 ± 2.2	15.4 ± 0.5	3.0	90	27.7 ± 2.8	18.0 ± 0.4	3.0	131	- 9.7
610	67.8 ± 2.2	17.5 ± 0.4	3.7	104	27.5 ± 2.5	20.8 ± 0.4	3.7	107	-10.3
630	71.6 ± 2.2	19.8 ± 0.4	4.5	139	28.3 ± 2.4	22.6 ± 0.5	4.5	139	-10.9
650	74.0 ± 2.3	24.2 ± 0.4	4.5	140	34.1 ± 2.6	26.5 ± 0.5	4.5	139	-11.5
670	67.3 ± 3.7	31.0 ± 0.4	4.5	98	47.8 ± 3.0	31.8 ± 0.5	4.5	99	-12.2
690	76.9 ± 2.9	36.9 ± 0.5	4.5	126	45.6 ± 2.4	38.2 ± 0.5	4.5	126	-12.8
710	80.6 ± 3.0	43.6 ± 0.5	4.5	141	54.4 ± 3.4	44.2 ± 0.6	4.5	146	-13.4
730	87.5 ± 3.3	56.5 ± 0.6	4.5	112	59.6 ± 3.3	57.2 ± 0.8	4.5	117	-14.0
750	89.0 ± 5.3	70.0 ± 1.2	4.5	149	72.7 ± 8.8	70.4 ± 1.5	4.5	150	-14.7
770									
790	83.8 ± 3.2	106.1 ± 1.7	4.5	134	113.2 ± 3.5	102.5 ± 1.8	4.5	140	-15.9
810	94.5 ± 4.3	118.6 ± 0.9	4.5	131	105.2 ± 5.8	117.5 ± 0.9	4.5	136	-16.5
830	90.3 ± 2.9	127.7 ± 0.8	4.5	133	122.2 ± 4.0	127.3 ± 1.3	4.5	134	-17.2
850	93.5 ± 3.1	135.0 ± 0.7	4.5	96	131.3 ± 3.0	133.8 ± 0.9	4.5	95	-17.8
870	89.2 ± 2.7	137.2 ± 0.6	4.5	110	140.7 ± 2.4	134.1 ± 0.8	4.5	112	-18.4
890	99.8 ± 4.1	143.6 ± 0.6	4.5	102	137.1 ± 2.4	141.5 ± 0.8	4.5	104	-19.1
910	99.1 ± 4.1	147.4 ± 1.1	3.4 ± 0.7	234	144.7 ± 2.6	145.2 ± 1.1	2.6 ± 0.7	235	-19.4
930	105.6 ± 2.5	151.7 ± 0.5	4.0 ± 0.5	256	132.5 ± 3.9	149.7 ± 0.5	5.3 ± 0.6	256	-20.0
950	108.7 ± 5.0	152.8 ± 1.1	3.7 ± 0.8	282	137.5 ± 4.2	150.6 ± 1.0	4.5 ± 0.7	278	-20.5
970	112.4 ± 10.0	156.3 ± 1.2	6.1 ± 1.2	183	143.3 ± 3.3	153.8 ± 0.9	6.5 ± 0.6	175	-20.9

By this means or by following the Barrelet zeros (see section 7, fig. 20) it is possible to keep track of the two solutions through the ρ mass region. The solutions are stable to changes of parametrization and to changes of the t-region over which the data are fitted. With the exception of Solution 2 below $M_{\pi\pi}$ = 650 MeV the solutions are also stable to reasonable variations of the input values of δ_S^2 and δ_D^0. The black dots and open circles of fig. 11 denote Solutions 1 and 2 respectively. For comparison we show by a dashed curve the solution obtained by Protopopescu et al.[24] from an analysis of $\pi^+p \to \pi^+\pi^-\Delta^{++}$ data.

In contrast to recent analyses[6,22,24], we obtain two acceptable solutions below (as well as above) the ρ mass. At low $M_{\pi\pi}$ the solutions have very different $|S|$ and therefore lead to different extrapolated ππ cross sections. However, both values are compatible with the physical region data since the non π exchange background differs for the two solutions in such a way as to give good fits to the data in each case. We discuss this further in the next section.

If we were to believe that the non-vanishing absorptive background [C(t) of eqn.(18)] is dominantly real relative to π exchange then this appears to favour the solution with the smaller $P_-^\perp$, that is, Solution 1. On the other hand, although the results of the phase coherent analysis ($P_-^\perp = 0$) described in the next section do in general prefer Solution 1, we find even there an acceptable Solution 2 at $M_{\pi\pi}$ values below and above the ρ mass region. In summary the $\pi^-\pi^+n$ data alone do not resolve the S-wave ambiguity in the elastic region.

The most direct way to select the physical solution is to study the $\pi^0\pi^0$ mass distribution[26,27], since here only even L ππ partial waves can contribute. The histogram in fig. 12 is the $\pi^0\pi^0$ mass spectrum for $2\mu^2 < -t < 8\mu^2$ obtained from a $\pi^-p \to \pi^0\pi^0n$ experiment[26] at 8 GeV/c. In terms of ππ phase shifts this spectrum is, to a good approximation, proportional to

$$\frac{d\sigma(\pi^0\pi^0)}{dM_{\pi\pi}} \propto \frac{M_{\pi\pi}^2}{q} \sum_{L=0,2} (2L+1) \left| 1/3\, f_L^0 - 1/3\, f_L^2 \right|^2$$

where the partial wave amplitudes, f_L^I, are defined as in eqn.(6). The predictions of the two solutions are shown on the figure. A comparison of the

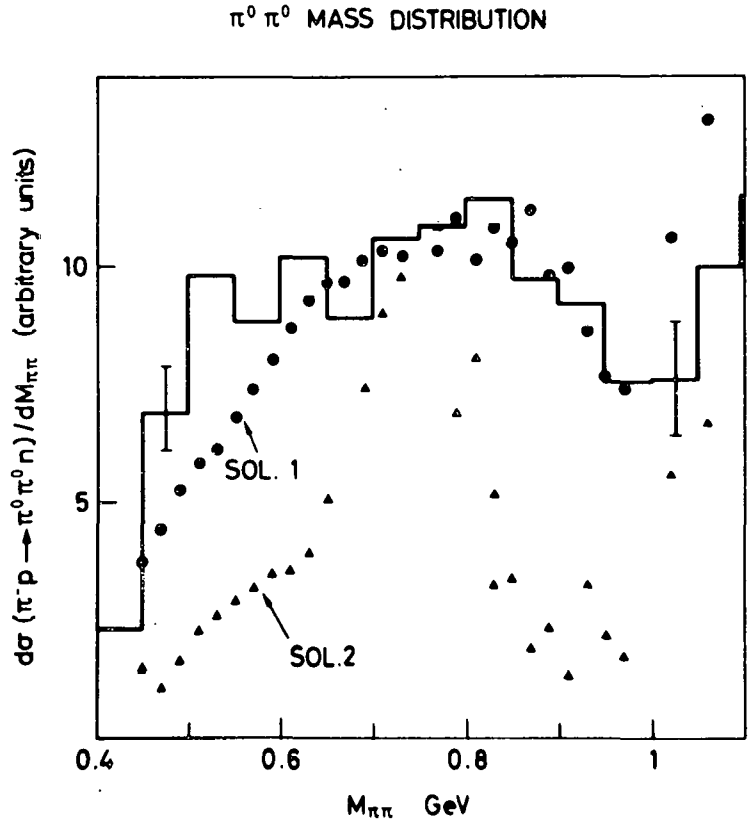

Fig. 12 The histogram is the $\pi^0\pi^0$ mass spectrum for $2\mu^2 < -t < 8\mu^2$ from $\pi^- p \to \pi^0\pi^0 n$ at 8 GeV/c[26]. The circles (triangles) are the shape of the spectrum calculated from the $\pi\pi$ phases of Solution 1 (Solution 2) respectively. The scale is arbitrary.

shapes of the mass spectrum clearly selects Solution 1 as the physical solution.

Above $M_{\pi\pi}$ = 920 MeV we allow the P-wave to be inelastic. Although $|f_P|$ is well determined, the inelasticity parameter η_P is poorly constrained by the data for $M_{\pi\pi} \sim 950$ MeV. The reason is apparent from fig. 13. The data determine $|f_P|$, $|f_S|$ and $\cos(\delta_S - \delta_P)$ but not the overall phase, and thus the solutions shown have comparable χ^2. The phase shifts listed assume that the P-wave is elastic below 1 GeV.

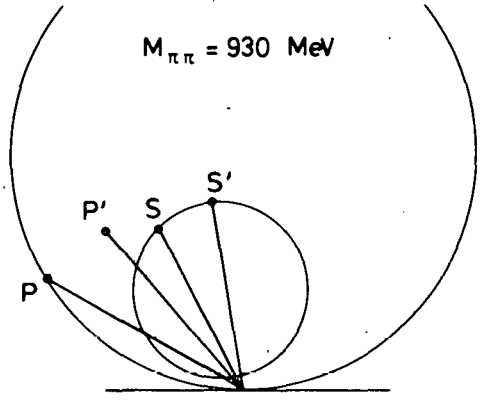

Fig. 13 S, P denote Solution 1 at $M_{\pi\pi}$ = 930 MeV. The solution S', P', with an inelastic P-wave gives a comparable fit to the data.

To determine resonance parameters we use the form[28]

$$f_L = \frac{x\, M_R\, \Gamma}{M_R^2 - M_{\pi\pi}^2 - i\, M_R\, \Gamma} \qquad (22)$$

with

$$\Gamma = \left(\frac{q}{q_R} \right)^{2L+1} \frac{D_L(q_R r)}{D_L(q r)}\, \Gamma_R$$

For the ρ we use $D_1(y) = 1 + y$ and fit to the P-wave phase shift of Solution 1 in the range $650 \leq M_{\pi\pi} \leq 890$ MeV. With this parametrization, we find for the ρ

$$M_\rho = 772.2 \pm 0.6 \text{ MeV}, \qquad \Gamma_\rho = 143.1 \pm 1.1 \text{ MeV}, \qquad r_\rho = 0.83 \pm 0.08 \text{ f}$$

5.2 D-Wave in the Elastic Region

In the ρ mass region the observed s-channel $\langle Y_0^3 \rangle$ moment has a systematic behaviour versus both $M_{\pi\pi}$ and t which is consistent with P - D interference. For a fixed t ∿ -0.05 GeV^2 the normalized $\langle Y_0^3 \rangle$ moment decreases from around 0.04 for $M_{\pi\pi}$ ∿ 600 MeV, through zero in the region of the ρ mass, to about -0.03 for $M_{\pi\pi}$ ∿ 900 MeV. For fixed $M_{\pi\pi}$ $\langle Y_0^3 \rangle$ reaches a maximum size for -t ∿ 0.05 and then decreases changing sign for -t ∿ 0.15 GeV^2. Examples of the observed s-channel $\langle Y_0^3 \rangle$ moment are shown in fig. 14.

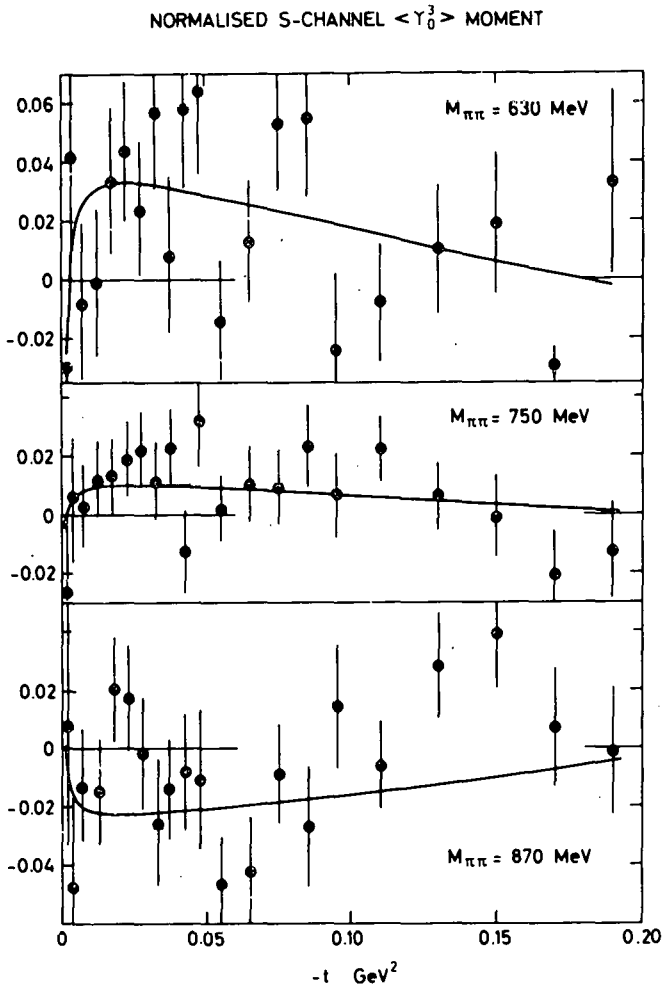

Fig. 14 The t dependence of the s-channel $\langle Y_0^3 \rangle$ moment in three typical 20 MeV $M_{\pi\pi}$ bins. The curves are the description of the data for $\delta_D^0 = 4.5^o$.

In terms of production amplitudes

$$\sqrt{4\pi}\, N \langle Y_0^3 \rangle = \frac{6}{\sqrt{35}} \mathrm{Re}\,(\sqrt{3}\, P_0 D_0^* - P_- D_{1-}^* - P_+ D_{1+}^*) \qquad (23)$$

$$\approx \frac{6\sqrt{3}}{\sqrt{35}} \left|\frac{D_0}{P_0}\right| \left[\, |P_0|^2 - |P_-|^2 - |P_+|^2 \,\right] \cos(\delta_P - \delta_D)$$

The last equality is obtained assuming the proportionality relation

$$D_{1\pm} = \sqrt{3}\, D_0\, (P_\pm/P_0) \qquad (24)$$

where the $\sqrt{3}$ arises from crossing the π exchange contribution to the s-channel. For instance such a relation is implied by the Williams model. In eqn.(23) the $M_{\pi\pi}$ behaviour of $\langle Y_0^3 \rangle$ arises mainly from the factor $\cos(\delta_P - \delta_D)$, while the t behaviour of $\langle Y_0^3 \rangle$ is due to the term in square brackets.

Knowing the P-wave amplitudes and taking the D-wave to be elastic below $M_{\pi\pi}$ = 900 MeV and dominantly I = 0 we calculate δ_D^0 for each $M_{\pi\pi}$ bin by comparing eqn.(23) with the $\langle Y_0^3 \rangle$ data. Over the entire range 620 MeV < $M_{\pi\pi}$ < 900 MeV we find δ_D^0 is essentially constant with a value of $\delta_D^0 = 4.5^\circ$. For mass values close to $M_{\pi\pi}$ = 780 MeV δ_D^0 cannot be reliably determined since the P- and D-amplitudes are about $\pi/2$ out of phase. That δ_D^0 should be so large for $M_{\pi\pi} \sim 650$ MeV is puzzling. The curves in fig. 14 are calculated from eqn.(23) using $\delta_D^0 = 4.5^\circ$. Equation (23) gives a good (one parameter) description of the $M_{\pi\pi}$ and t behaviour of the $\langle Y_0^3 \rangle$ moment. Versus $M_{\pi\pi}$ it predicts a $\langle Y_0^3 \rangle$ sign change at $M_{\pi\pi} \sim 780$ MeV (the data cross-over is at $M_{\pi\pi} \sim 800$ MeV) and versus t a sign change at $-t \sim 0.2$ (compared to 0.15 in the data).

In the S- and P-wave phase analysis in the region 620 < $M_{\pi\pi}$ < 900 MeV we took $\delta_D^0 = 4.5^\circ$. Below 620 MeV the estimates of δ_D^0 may not be reliable, since for $M_{\pi\pi} \lesssim 500$ MeV an anomalous behaviour is observed in some higher moments[4], and therefore we assumed a q^5 threshold behaviour of δ_D^0. For $M_{\pi\pi}$ > 900 MeV we included the J = 3,4 moments and determined δ_D^0 in each mass bin.

6 PHASE COHERENT ANALYSIS

We repeated the $\pi\pi$ phase shift analysis using essentially a Williams' model parametrization of the production amplitudes. In place of eqns.(18), we use the simplified forms

$$P_0 = -\frac{g_\pi}{\sqrt{q}}\, M_{\pi\pi}\, \frac{\sqrt{-t'}}{t - \mu^2}\, e^{b(t - \mu^2)} \qquad (25)$$

$$P_- = \frac{g_\pi}{\sqrt{q}} \left[\frac{2t'}{t - \mu^2} - C \right] e^{b(t - \mu^2)}$$

$$P_+ = - \frac{g_\pi}{\sqrt{q}} C e^{b(t - \mu^2)} \qquad (25)$$

where C, which specifies the absorptive background, is assumed to be real and independent of t. Strictly speaking the Williams' model has C = 1, however, here we take C as a parameter to be determined in each mass bin. Departures from the above simple parametrization occur for $-t \gtrsim 0.15$ GeV^2 due to the neglect of A_2 exchange contributions, etc[15]. Therefore we restrict the analysis to the data in the region $-t < 0.1$ GeV^2. The points shown in fig. 15 for $M_{\pi\pi} <$ 1 GeV are the results of this analysis. The values of δ_S^0 are in excellent agreement with Solution 1 of section 5 and are a demonstration of the stability of the phase shifts to a change of parametrization.

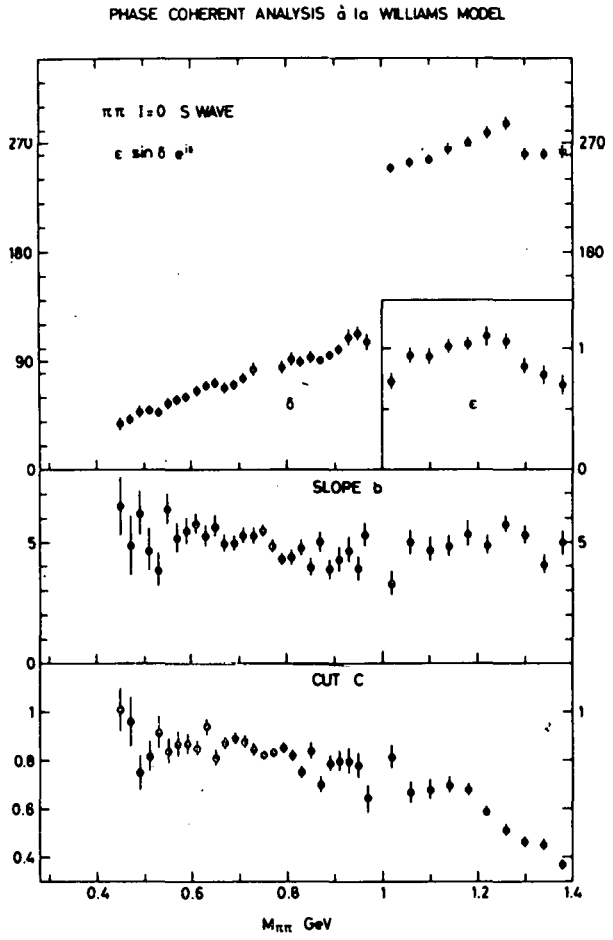

Fig. 15 Some results of a phase shift analysis using a simplified parametrization, eqns.(25). The results above 1 GeV are discussed in section 7.4.

Since phase coherence between P_0 and P_- is an input assumption here, it is not surprising that we obtain Solution 1. However, for mass bins where the two solutions of section 5 are dissimilar (i.e., away from the region of the ρ mass) we also find Solution 2, and with comparable χ^2. Moreover the values of C are almost identical for the two solutions, whereas for $M_{\pi\pi} \sim 500$ MeV we have already remarked (cf. section 5) that the background has to be different for the two solutions. This apparent contradiction is resolved when we note that δ_P is significantly different for the two solutions in this mass region.

7 PHASE SHIFT ANALYSIS IN THE INELASTIC REGION

Above the $K\bar{K}$ threshold we cannot impose elastic unitarity. Indeed, the $\pi\pi \to K\bar{K}$ cross section is observed[24,29] to rise rapidly to its S-wave unitarity limit. Further we can no longer regard the D-wave as a small correction. On the other hand we still want to perform a phase shift analysis at each $M_{\pi\pi}$ independently. We use a similar method to that described in sections 4 and 5.

7.1 Production Amplitude Analysis

From the observed s-channel moments with $J, M \leq 4$ we determine the production amplitudes $L_{\lambda\pm}$ with $L, \lambda \leq 2$, and extrapolate S, P_0, D_0 to the π exchange pole. The data determine the magnitudes and relative phases of S, P_0, D_0, but not the overall phase. In the elastic region unitarity determined the overall phase, but in the inelastic region the unitarity constraint is weaker. For example a solution such as shown in fig. 16 can be rotated through any angle provided that the partial waves lie within their unitarity circles.

We have tried several different forms of parametrization of the s-channel amplitudes. As in the elastic region we find that, as long as we include the $\lambda \neq 0$ amplitudes, the phase shifts are stable to changes of the form of the parametrization and to changes of the t interval over which the moments are fitted. The results we present are based on the parametrizations of eqns.(18) with the additional assumptions

$$D_{1\pm} = \sqrt{3}\, P_{\pm} \frac{D_0}{P_0} \tag{26}$$

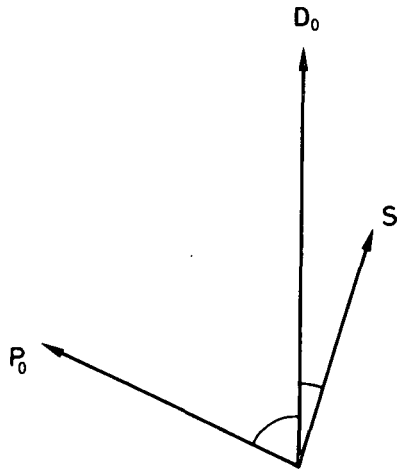

Fig. 16 Dominant π exchange amplitudes. Only the magnitudes and relative phases are determined.

$$D_{2\pm} = \frac{\sqrt{-t'}}{M_{\pi\pi}} D_{1\pm} \tag{27}$$

which are motivated by studying the t- to s-channel crossing matrix. Equations (26) and (27) are correct provided the main contribution to the s-channel $\lambda = 1,2$ amplitudes is due to π exchange and its absorptive correction. This is expected to be a good approximation for $-t < 0.2$ GeV^2, particularly as A_2 exchange decreases* relative to π exchange with increasing $M_{\pi\pi}$.

In the region $1.0 < M_{\pi\pi} < 1.4$ GeV we used data[4] in 40 MeV mass bins. In each mass bin we fitted the s-channel moments with $J \leq 4$ in the interval $0 < -t < 0.2$ GeV^2. A typical fit is shown in fig. 17. The two solutions have comparable χ^2 but have different magnitudes and relative phases of S, P_0 and D_0. We parametrize the partial wave amplitudes f_L of eqn.(8), in the form

$$f_L = \begin{cases} r_L \, e^{i\delta_L} & \text{for} \quad L = 1 \\ 2/3 \, r_L \, e^{i\delta_L} & \text{for} \quad L = 0, 2 \end{cases} \tag{28}$$

and fix the overall phase by the choice $\delta_D = 90^\circ$. The 2/3 is inserted for even L so that, if there were no I = 2 $\pi\pi$ amplitude, unitarity would require

*For instance, for $-t \gtrsim 0.4$ GeV^2 the moments indicate that the natural parity exchange contribution is less dominant in the f region than in the ρ region.

TABLE 3

The $\pi\pi$ partial wave amplitudes, f_L of eqn.(28), obtained in the analysis of reaction $\pi^- p \to \pi^-\pi^+ n$ in the region $1.0 < M_{\pi\pi} < 1.4$ GeV. The overall phase is fixed by the choice $\delta_0 = 90^\circ$. In each 40 MeV mass bin we fit 15 moments at 19 t values in the range $0 < -t < 0.2$ GeV^2. Solution 1 is the physical solution.

$M_{\pi\pi}$	Solution 1						Solution 2					
(GeV)	r_S	δ_S	r_P	δ_P	r_D	x^2	r_S	δ_S	r_P	δ_P	r_D	x^2
1.02	0.74 ± 0.10	146 ± 2	0.32 ± 0.02	212 ± 2	0.21 ± 0.02	324	0.16 ± 0.03	193 ± 4	0.42 ± 0.01	201 ± 2	0.21 ± 0.02	327
1.06	0.81 ± 0.08	146 ± 2	0.33 ± 0.02	213 ± 2	0.24 ± 0.02	286	0.22 ± 0.05	190 ± 22	0.45 ± 0.01	203 ± 2	0.24 ± 0.02	296
1.10	1.01 ± 0.04	149 ± 2	0.27 ± 0.01	218 ± 2	0.32 ± 0.01	348	0.28 ± 0.04	168 ± 8	0.45 ± 0.01	203 ± 2	0.32 ± 0.01	364
1.14	1.08 ± 0.05	148 ± 2	0.22 ± 0.02	211 ± 2	0.39 ± 0.01	273	0.32 ± 0.04	157 ± 5	0.45 ± 0.01	195 ± 1	0.39 ± 0.01	277
1.18	1.13 ± 0.06	145 ± 2	0.27 ± 0.03	207 ± 2	0.54 ± 0.02	268	0.62 ± 0.10	140 ± 3	0.44 ± 0.04	197 ± 2	0.54 ± 0.02	274
1.22	1.23 ± 0.06	136 ± 2	0.22 ± 0.03	195 ± 2	0.69 ± 0.01	266	0.86 ± 0.10	127 ± 4	0.40 ± 0.04	189 ± 4	0.69 ± 0.01	272
1.26	1.11 ± 0.06	121 ± 3	0.23 ± 0.03	171 ± 5	0.82 ± 0.02	353	1.21 ± 0.05	126 ± 3	0.15 ± 0.03	164 ± 6	0.81 ± 0.02	348
1.30	1.02 ± 0.06	99 ± 5	0.32 ± 0.03	163 ± 2	0.78 ± 0.02	327	1.29 ± 0.03	122 ± 3	0.10 ± 0.03	116 ± 7	0.78 ± 0.02	319
1.34	0.94 ± 0.08	83 ± 6	0.32 ± 0.03	150 ± 4	0.66 ± 0.02	292	1.17 ± 0.05	116 ± 5	0.19 ± 0.03	61 ± 14	0.66 ± 0.01	286
1.38	0.93 ± 0.09	81 ± 10	0.31 ± 0.04	144 ± 6	0.57 ± 0.02	307	1.14 ± 0.04	118 ± 5	0.20 ± 0.02	64 ± 11	0.56 ± 0.02	311

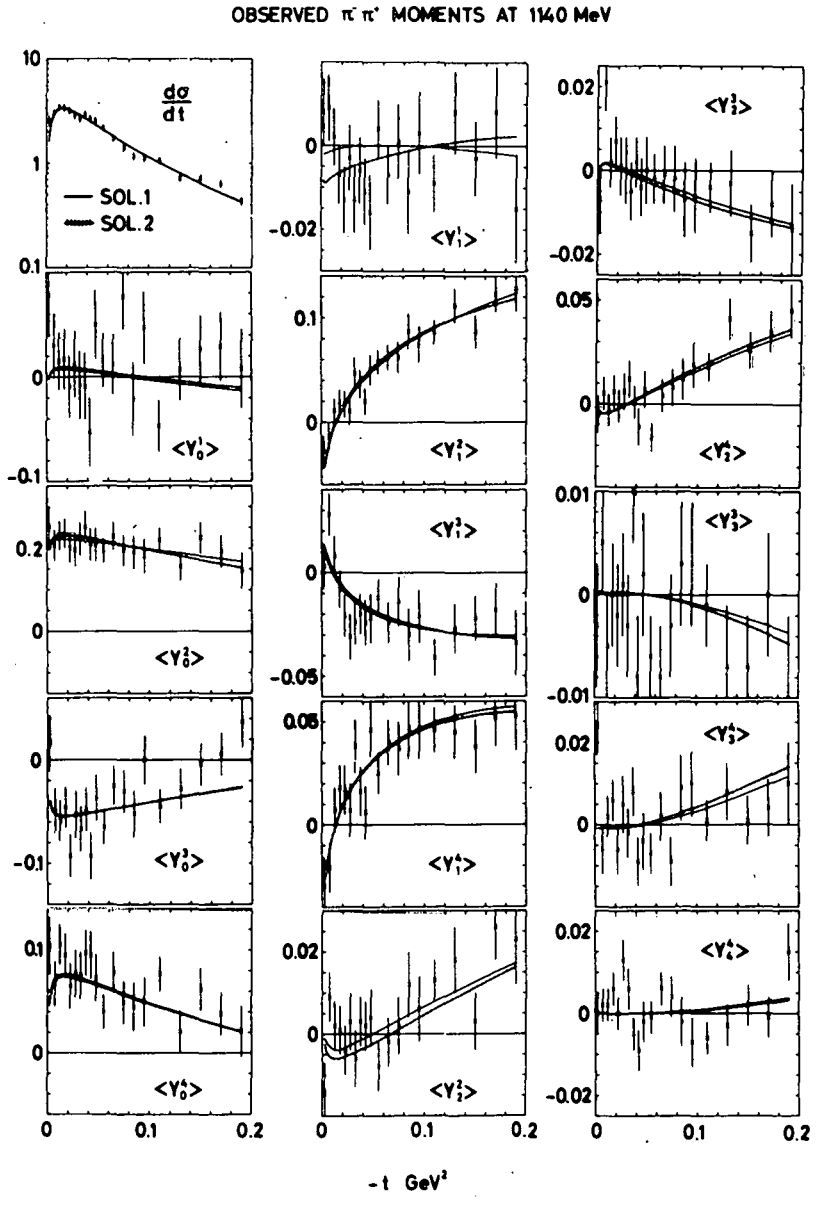

Fig. 17 The fits to the s-channel moments in a typical mass bin, $1.12 < M_{\pi\pi} < 1.16$ GeV. The partial wave parameters are given in Table 3.

$r_L \leq \sin\delta_L$. This bound is not imposed in the fit to the data. The results for each 40 MeV mass bin are listed in Table 3. In fig. 18 they are shown in the form $\sqrt{2L+1}\, f_L$, which represents their relative strength in the production process. We must now explain why we have shown two solutions.

7.2 Zero Contours

In addition to the continuum ambiguity of the overall phase are there discrete ambiguities in the phase shift analysis? Yes, for S, P, D-waves there

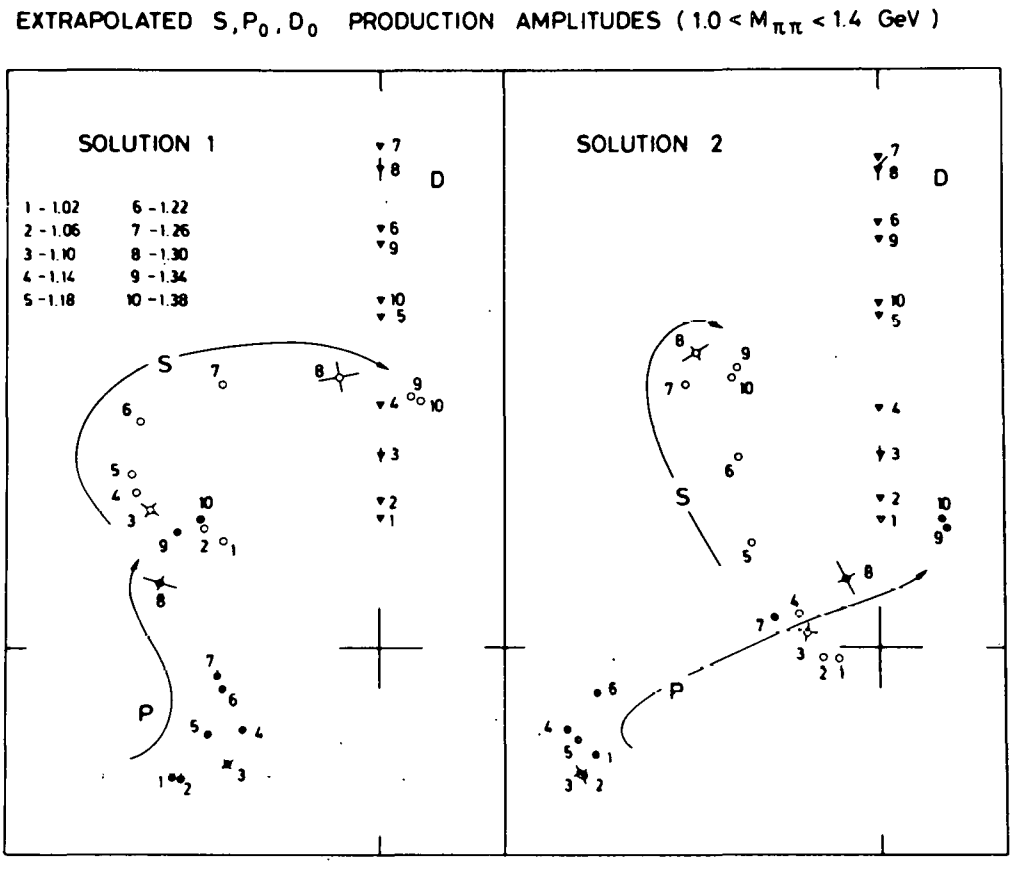

Fig. 18 Two solutions for the $\pi^+\pi^-$ partial wave amplitudes f_L (scaled by $\sqrt{2L+1}$) found by analyzing $\pi^-p \to \pi^-\pi^+n$ data in 40 MeV mass bins in the range $1.0 < M_{\pi\pi} < 1.4$ GeV. We choose $\delta_D = 90^\circ$. Typical errors are shown at $M_{\pi\pi} = 1.1$ and 1.3 GeV. The results are listed in Table 3.

are four solutions giving identical $d\sigma_{\pi\pi}/d\Omega$. A useful way[30,31] of seeing this and of keeping track of the four solutions is to study the zeros of the $\pi^+\pi^-$ scattering amplitude in the complex $z \equiv \cos\theta_{\pi\pi}$ plane. These have been called Barrelet zeros[32]. For S, P, D-waves the $\pi\pi$ amplitude A(z) will have two such zeros, say at $z = z_1$ and $z = z_2$. Thus,

$$\frac{d\sigma_{\pi\pi}}{d\Omega} = A(z)\,A^*(z^*) = C(z - z_1)(z - z_2)(z - z_1^*)(z - z_2^*) \quad (29)$$

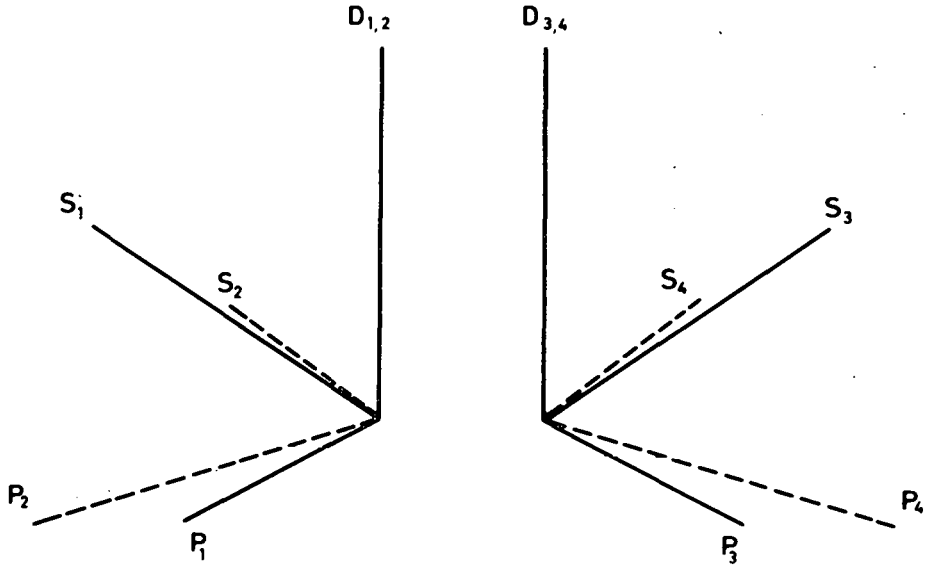

Fig. 19 The four solutions at $M_{\pi\pi}$ = 1.18 GeV.

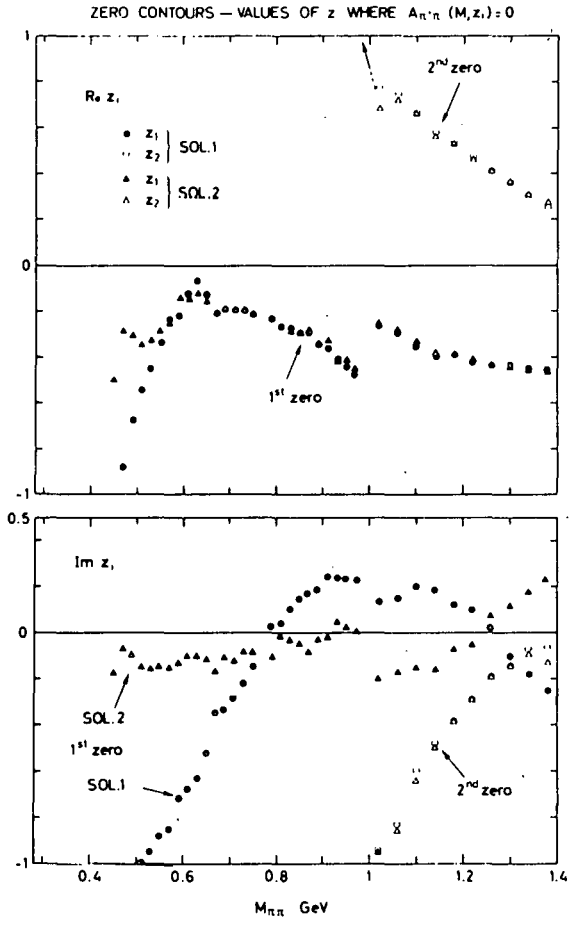

Fig. 20 The positions of the zeros, $z = z_i$, of the $\pi^+\pi^-$ amplitude as calculated from the two partial wave solutions listed in Tables 2 and 3. z is the cosine of the $\pi\pi$ c.m. scattering angle.

and for each z_i there is a two-fold ambiguity. Is $z = z_i$ or $z = z_i^*$ the zero of A? For example, at $M_{\pi\pi} = 1.18$ GeV from Solution 1 of fig. 19 we calculate the zeros and predict the other three solutions that are shown. Having obtained one solution the procedure is to use these three predictions as starting values in the analysis of the observed moments. In this way we obtain four solutions at each $M_{\pi\pi}$. Two of the solutions (those denoted Solutions 3 and 4 in the example shown in fig. 19) are clearly ruled out by studying continuity of the partial waves with $M_{\pi\pi}$. The real and imaginary parts of the positions of the zeros for the other two solutions are shown in fig. 20. By following the zero contours we can keep track of the solutions. However, two similar solutions exist whenever Im $z_i \approx 0$. For example for $M_{\pi\pi} \gtrsim 1.26$ GeV we have to use continuity of the zeros to decide which is Solution 1 and which is Solution 2. We also see that Solutions 3 and 4 will need to be considered for $M_{\pi\pi} > 1.4$ GeV as Im z_2 is becoming small.

The actual solutions need not have exactly complex conjugate zeros, since, for example, the predicted absorption in the production process may differ for the solutions and so lead to a different extrapolated $\pi\pi$ cross section, $d\sigma_{\pi\pi}/d\Omega$. Absorption decreases rapidly with $M_{\pi\pi}$ and in the region above 1 GeV we do, in fact, have solutions with approximately complex conjugate zeros. In fig. 20 we also show the positions of the zeros obtained from the phase shifts in the elastic region. The two solutions there are not, in general, due to complex conjugate zeros, but arise because the production amplitude analysis leads to different extrapolated $d\sigma_{\pi\pi}/d\Omega$. For example, at $M_{\pi\pi} \approx 600$ MeV there are two solutions with Im $z_1 > 0$ but with partial waves that do not satisfy unitarity.

It is illuminating to draw the contours of Re z_i on the Mandelstam plot. They are shown in fig. 21. The continuation of the contour z_1 towards the Mandelstam triangle has been associated[33] with the on-shell appearance of the Adler zero. The contour z_2 is reasonably consistent with the proposal by Odorico[8] that the double pole killing zeros propagate along straight lines.

7.3 $\pi\pi$ Partial Waves

To determine the $\pi\pi$ partial waves in the inelastic region it remains to specify the overall phase at each $M_{\pi\pi}$. The possible values are limited by the unitarity constraints on the three partial waves. Moreover each partial wave

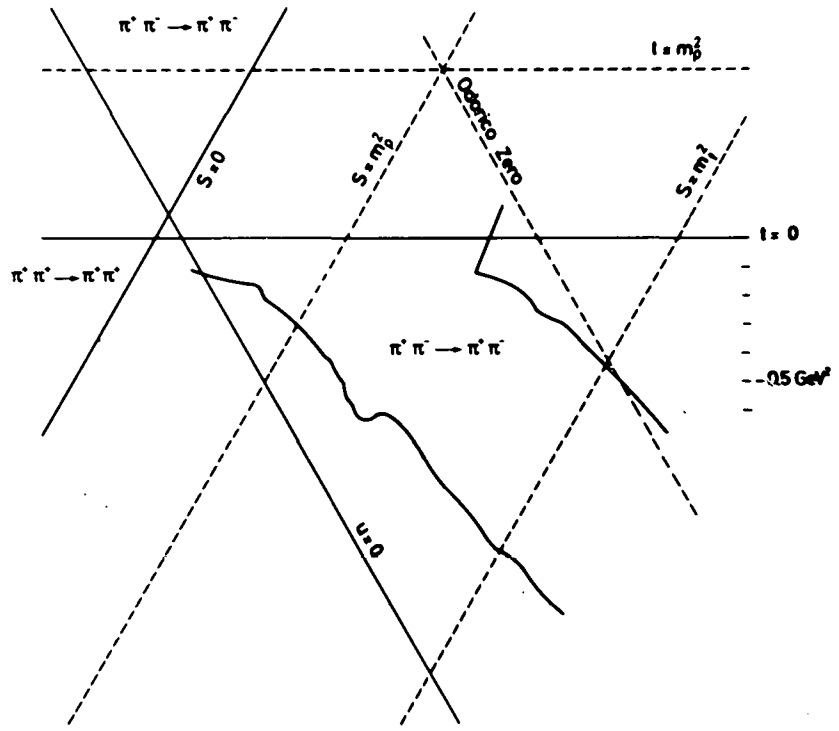

Fig. 21 The zero contours in the Mandelstam plot.

must be reasonably continuous as a function of $M_{\pi\pi}$. Indeed, the presence of the f resonance in this mass region essentially removes the phase ambiguity. Suitably rotating the two solutions of fig. 18 we obtain the partial waves shown in figs. 22 and 23, together with their unitarity circles. Solution 1 is selected as the physical solution for the following reasons. In the region just above the $K\bar{K}$ threshold the I = 0 S-wave of Solution 2 contributes very little to $\sigma(\pi\pi \to K\bar{K})$ contrary to the data. Further, the M matrix fits across the $K\bar{K}$ threshold prefer to join Solution 1 to the physical solution below threshold. Finally, for $M_{\pi\pi} > 1.26$ GeV the magnitude of the S-wave of Solution 2 violates unitarity.

Notice that in fig. 22 the P-wave lies outside its unitarity circle for $M_{\pi\pi} \gtrsim 1.26$ GeV. The reason we believe that the picture is basically correct as it stands, apart from this violation, is the neglect of the $\pi\pi$ F-wave. The data that we used did not include the J = 5 or higher moments and so we were unable to determine the L = 3 partial wave. On the other hand we investigated the stability of the analysis to the inclusion of elastic F-waves with $\delta_F \lesssim 5^\circ$.

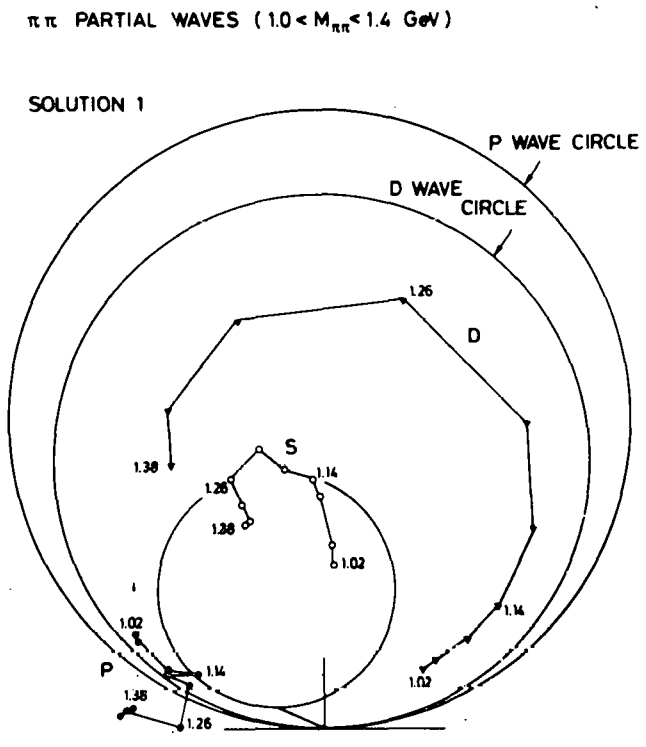

Fig. 22 The physical solution, Solution 1, for the $\pi\pi$ partial wave amplitudes above 1 GeV. The I = 0 S-wave, P-wave and I = 0 D-wave unitarity circles are in the ratio $2/3 : \sqrt{3} : 2/3\sqrt{5}$.

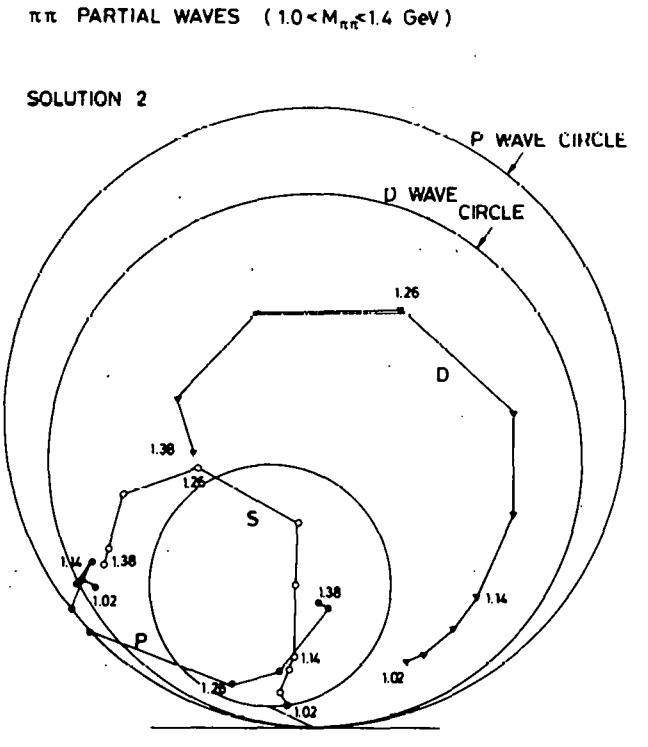

Fig. 23 The $\pi\pi$ partial waves for the unphysical solution, Solution 2.

We find that the D-wave is essentially unchanged and that the S-wave is only slightly altered. The major change is in the P-wave which decreases and rotates in the clockwise direction (for example, for $\delta_F = 4^\circ$ at $M_{\pi\pi} = 1.38$ GeV, we find $\Delta\,\delta_P = -10^\circ$ and $\Delta r_P/r_P = -0.12$).

To determine the parameters of the f resonance we fit the resonance form, eqn.(22) with

$$D_2(y) = 9 + 3y + y^2 ,$$

to the values of $|r_D|$ in the region $1.14 < M_{\pi\pi} < 1.38$ GeV. Since $|r_D|$ is well determined and independent of the overall phase this procedure should be reliable. We find

$$M_f = 1271 \pm 2 \text{ MeV}, \qquad \Gamma_f = 182 \pm 4 \text{ MeV}$$
$$x_f = 0.81 \pm 0.01, \qquad r_f = 0.70 \pm 0.08\,\text{f}.$$

Figure 22 also indicates the presence of a resonant I = 0 S-wave under the f, with a mass and width of roughly 1240 and 200 MeV respectively. To confirm these parameters we wish to include F-waves and to extend the analysis to higher $M_{\pi\pi}$.

7.4 Phase Coherent Analysis

As in the elastic region we have performed a phase shift analysis with a simplified form of parametrization, cf. eqns.(25). We neglect A_2 exchange and assume that the absorptive background C is real relative to π exchange. We include a common slope factor, $\exp\left[b(t - \mu^2)\right]$, in all amplitudes. In addition to the parameters C and b we have the magnitudes and relative phases of the S, P, D partial waves. In each 40 MeV mass bin these seven parameters give a good fit to the s-channel moments in the region $0 < -t < 0.1$ GeV^2. The results for C, b and the I = 0 S-wave are shown in fig. 15, where the overall phase has been fixed by requiring the P-wave to be elastic. The partial waves are very similar to the Solution 1 results of fig. 22. Moreover we also find a solution almost identical to Solution 2.

A surprising result[34,35] is the rapid decrease of the strength of absorption, C, with increasing $M_{\pi\pi}$. This could be anticipated from the data by inspection of the positions of the cross-over zeros in the s-channel Y_1^J moments. For example comparing the moments shown at $M_{\pi\pi}$ = 710 MeV (fig. 10) and at $M_{\pi\pi}$ = 1140 MeV (fig. 17) we see that at the higher mass the zeros occur at smaller $|t|$. The Williams model, with C = 1, is known[36,15] to give a good description of the small t data in the ρ region, but is unsatisfactory in the f region.

8 S^* REGION

The data and the phase shift results indicate a dramatic effect in the I = 0 S-wave in the region of the $K\bar{K}$ threshold. Moreover the effect occurs in a small range of $M_{\pi\pi}$. Up to 980 MeV and beyond 1 GeV the partial wave amplitudes do not change rapidly, and yet in between the I = 0 S-wave amplitude has altered drastically. Clearly to investigate this effect properly we require the moments for $\pi^-p \to \pi^-\pi^+n$, together with those for $\pi^-p \to K^-K^+n$ (and $K_1^0K_1^0n$), in smaller $M_{\pi\pi}$ bins. However, even a study of the existing data and phase shifts is illuminating.

First we performed an S, P, D-wave M matrix fit directly on the data in the region 920 < $M_{\pi\pi}$ < 1080 MeV. That is we parametrized the production amplitudes as a function of $M_{\pi\pi}$, as well as of t. We did fits with and without effective range terms in the M matrix. As an alternative approach we also fitted the I = 0 S-wave phase shifts (cf. figs. 18, 22, 23) to an M matrix over the same $M_{\pi\pi}$ region. We discuss the results of the second method first. The preferred fit was the one which joined the phase shifts of Solution 1 below the $K\bar{K}$ threshold to those of Solution 1 above threshold. An example of such a fit is shown in fig. 24, corresponding to an I = 0 two channel ($\pi\pi$, $K\bar{K}$) M matrix

$$M = \begin{pmatrix} 0.27 & 0.83 \\ 0.83 & -0.09 \end{pmatrix} \text{fermi}^{-1} \qquad (30)$$

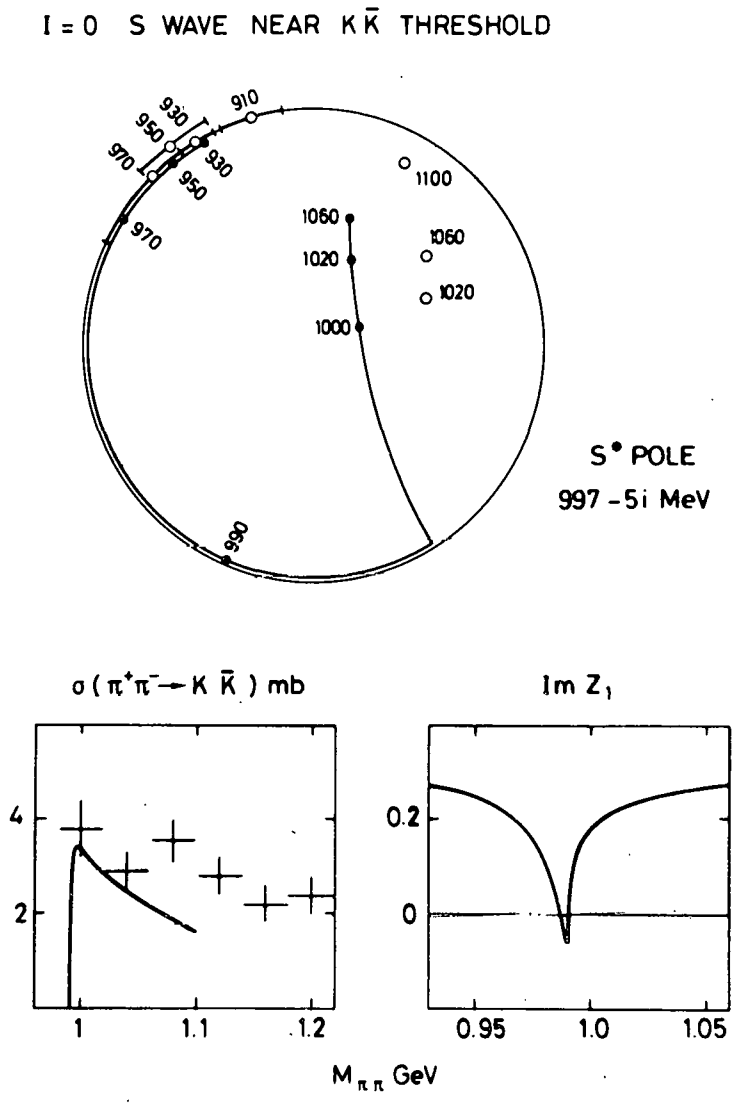

Fig. 24 The I = 0 S-wave unitarity circle. The open circles are Solution 1 of the energy independent analysis. The black dots come from the sample M matrix fit. The last curve is the behaviour of Im z_i (cf. fig. 20) calculated using the M matrix and assuming that $\delta_S^2 = -20^\circ$, $\delta_P = 156^\circ$, $\delta_D^0 = 6^\circ$.

The resulting S-wave amplitude has a pole on the second Riemann sheet of the complex energy plane at

$$S^*(\text{pole}) = 997 - i\,5 \text{ MeV}. \qquad (31)$$

The existence of such a pole was suggested by Hoang[37] and subsequently confirmed by Protopopescu et al.[24] whose favoured solution gives $S^* = 997 - i27$ MeV. In fig. 24 we compare the S-wave contribution to $\sigma(\pi^+\pi^- \to K\bar{K})$, calculated from eqn.(30), to the data of ref. 24. The narrower the peak in this cross section, the larger the S^* coupling to the $K\bar{K}$ channel[9].

It is interesting to compare the above results with our M matrix fit directly to the data. There we find a wider S^* structure. The reason is that, although the fit basically follows phase shift Solution 1, it jumps to Solution 2 for a range of $M_{\pi\pi}$ in the immediate vicinity of the $K\bar{K}$ threshold. This is likely to happen in any energy dependent fit to such a narrow structure, and is well illustrated in fig. 11 where the solution of Protopopescu et al.[24] goes from the region of our Solution 1 to Solution 2 just below the $K\bar{K}$ threshold. For this reason we believe that such fits can give misleading S^* parameters.

The rapidly changing S partial wave in the region of the $K\bar{K}$ threshold produces a sharp structure in the zero contours. For example, in fig. 24 we show the behaviour of Im z_1 calculated using the parameters of eqn.(30) and reasonable constant values for the other phase shifts. In the energy dependent fit Im z_1 is found to dip to zero less sharply. Comparison with the energy independent results of fig. 20 again emphasizes the need for data in smaller $M_{\pi\pi}$ bins in this mass region.

Since we predict such a small width for the S^* it is clear that the parameters of eqns.(30) and (31) are not reliably determined from the data in 20 - 40 MeV mass bins. However, the point we wish to make is that the S^* structure is probably much narrower than hitherto thought. An accurate determination of its parameters must await more data.

REFERENCES

1. P. Estabrooks, A.D. Martin, G. Grayer, B. Hyams, C. Jones, P. Weilhammer, W. Blum, H. Dietl, W. Koch, E. Lorenz, G. Lütjens, W. Männer, J. Meissburger, W. Ochs and U. Stierlin, to be published in Proc. Int. Conf. on $\pi\pi$ Scattering and Associated Topics, Tallahassee, 28 - 30 March, (1973).
2. C. Goebel, Phys. Rev. Letts. 1 (1958) 337; G.F. Chew and F.E. Low, Phys. Rev. 113 (1959) 1640.

3. See, for example, the review articles by:
P.E. Schlein, Proc. Int. School of Subnuclear Physics, Erice (1970);
J.L. Petersen, Phys. Reports 2C (1971) 157;
D. Morgan, Proc. VII Finnish Summer School in Theoretical Physics, Loma-Koli, 26 June - 7 July, 1972, ed. R. Pellinen (Helsinki, University of Helsinki, 1972).

4. CERN-Munich Collaboration: G. Grayer, B. Hyams, C. Jones, P. Schlein, P. Weilhammer, W. Blum, H. Dietl, W. Koch, E. Lorenz, G. Lütjens, W. Männer, J. Meissburger, W. Ochs and U. Stierlin, to be published.

5. G. Grayer et al., 3rd Int. Conf. on Experimental Meson Spectroscopy, Philadelphia, 28 - 29 April, 1972, Am. Inst. Phys. Conf. Proc. No. 8 (1972) 5.

6. G. Grayer et al., Phys. Letts. 35B (1971) 610.

7. J.T. Carroll et al., Phys. Rev. Letts. 28 (1972) 318.

8. R. Odorico, Phys. Letts. 38B (1972) 411.

9. S.M. Flatté, et al., Phys. Letts. 38B (1972) 232.

10. G.L. Kane and M. Ross, Phys. Rev. 177 (1969) 2353;
C.D. Froggatt and D. Morgan, Phys. Rev. 187 (1969) 2044;
G.L. Kane, Experimental Meson Spectroscopy, ed. C. Baltay and A.H. Rosenfeld (New York, Columbia University Press, 1970), p.1.

11. A. Kotański and K. Załewski, Nucl. Phys. B4 (1968) 559;
Nucl. Phys. B20 (1970) 236E; B22 (1970) 317.

12. J.D. Jackson and C. Quigg, Nucl. Phys. B22 (1970) 301.

13. W. Männer, Contribution to Int. Conf. on $\pi\pi$ Scattering and Associated Topics, Tallahassee, 28 - 30 March, 1973.

14. G. Grayer et al., Nucl. Phys. B50 (1972) 29.

15. P. Estabrooks and A.D. Martin, Phys. Letts. 41B (1972) 350.

16. See, for example, M. Ross, F.S. Henyey and G.L. Kane, Nucl. Phys. B23 (1970) 269.

17. C. Michael, Springer Tracts in Modern Physics, 55 (1970) 174.

18. P.K. Williams, Phys. Rev. D1 (1970) 1312.

19. C.D. Froggatt and D. Morgan, Phys. Letts. 40B (1972) 655.

20. J.D. Kimel and E. Reya, Phys. Letts. 42B (1972) 249.

21. W. Hoogland, Contribution to the Int. Conf. on $\pi\pi$ Scattering and Associated Topics, Tallahassee, 28 - 30 March, 1973.

22. P. Baillon et al., Phys. Letts. 38B (1972) 555.

23. J.P. Baton, G. Laurens and J. Reignier, Phys. Letts. 33B (1970) 525 and 528.

24. S.D. Protopopescu et al., Phys. Rev. D7 (1973) 1279.

25. See, for example, G.C. Fox, 3rd Int. Conf. on Experimental Meson Spectroscopy, Philadelphia, 28 - 29 April, 1972, Am. Inst. Phys. Conf. Proc. No. 8 (1972).

26. W.D. Apel et al., Karlsruhe-Pisa Collaboration, Contribution to XVI Int. Conf. on High Energy Physics, Batavia (1972).

27. A. Skuja et al., LBL Preprint 1020, March, 1973.

28. A. Barbaro-Galtieri, Advances in Particle Physics (Wiley, New York, 1968).

29. W. Beusch, Experimental Meson Spectroscopy, ed. C. Baltay and A.H. Rosenfeld (New York, Columbia University Press, 1970) p.185.

30. A. Gersten, Nucl. Phys. B12 (1969) 537.

31. E. Barrelet, Nuovo Cim. 8A (1972) 331.

32. C. Schmid, Proc. 1971 Amsterdam Int. Conf. on Elementary Particles (Amsterdam, North Holland, 1972) p.275.

33. M. Pennington and C. Schmid, Berkeley Preprint LBL-1005 (1972).

34. W. Ochs and F. Wagner, to be published in Nucl. Phys.

35. A.D. Martin and P. Estabrooks, to be published in Proc. of VIII Rencontre de Moriond (1973).

36. P. Baillon et al., Phys. Letts. 35B (1971) 453.

37. F.T. Hoang, Nuovo Cim. 61A (1969) 325.